Multiphoton Absorption Stimulated Metal Chalcogenide Quantum Dot Solar Cells Under Ambient and Concentrated Irradiance

Bo Hou[1,‡], Byung-Sung Kim[2,‡], Harrison K. H. Lee[3], Yuljae Cho[4], Paul Giraud[2], Mengxia Liu[5,§], Jingchao Zhang[6], Matthew L. Davies[3], James R. Durrant[3,7], Wing C. Tsoi[3], Zhe Li[8], Stoichko Dimitrov[9], Jung Inn Sohn[10*], SeungNam Cha[11*] and Jong Min Kim[12]*

1. Department of Physics and Astronomy, Cardiff University, Cardiff CF24 3AA, United Kingdom
2. Department of Engineering Science, University of Oxford, OX1 3PJ, Oxford, United Kingdom
3. SPECIFIC, College of Engineering, Swansea University, SA1 8EN, Swansea, United Kingdom
4. University of Michigan-Shanghai Jiao Tong University Joint Institute, Shanghai Jiao Tong University, 800 Dong Chuan Road, Minhang District, Shanghai 200240, China
5. Department of Electrical and Computer Engineering, University of Toronto, 10 King's College Road, Toronto, Ontario M5S 3G4, Canada
6. Department of Biostatistics and Bioinformatics, Emory University, Atlanta, GA, 30322, USA
7. Department of Chemistry, Imperial College London, SW7 2AZ, London, United Kingdom
8. School of Engineering and Materials Science (SEMS), Queen Mary University of London, E1 4NS, London, United Kingdom
9. School of Biological and Chemical Sciences, Queen Mary University of London, E1 4NS, London, United Kingdom
Email: s.dimitrov@qmul.ac.uk (S.D.)
10. Division of Physics and Semiconductor Science, Dongguk University, Seoul 100-715, Republic of Korea
Email: junginn.sohn@dongguk.edu (J.I.S)
11. Department of Physics, Sungkyunkwan University, Suwon, 16419, Republic of Korea
Email: chasn@skku.edu (S.C.)
12. Department of Engineering, University of Cambridge, CB3 0FA, Cambridge, United Kingdom
‡ These authors contributed equally to this work.
§ Present address: Cavendish Laboratory, University of Cambridge, J. J. Thomson Avenue, Cambridge, CB3 0HE, United Kingdom

Abstract

Colloidal metal chalcogenide quantum dots (QDs) have excellent quantum efficiency in light-matter interactions and good device stability. Although, QDs have been brought to the forefront as viable building blocks in bottom-up assembling semiconductor devices, the development of QD solar cell (QDSC) is still confronting considerable challenges comparing to other QD technologies due to their low performance under natural sunlight, as a consequence of untapped potential from their quantized density-of-state and inorganic natures. This report is designed to address this long-standing challenge by accessing the feasibility of using QDSC for indoor and concentration PV (CPV) applications. This work finds above bandgap photon energy irradiation of QD solids can generate high densities of excitons via multi-photon absorption (MPA) and these excitons are not limited to diffuse by Auger recombination up to 1.5×10^{19} cm^{-3} densities irradiance. Based on these findings, a 19.5% (2000 lux indoor light),

and an 11.6% efficiency (1.5 Suns) have been facilely realized from an ordinary QDSCs (9.55% under 1 Sun). To further illustrate the potential of the MPA in QDSCs, a 21.29% efficiency polymer lens CPVs (4.08 Suns) and viable sensor networks powered by indoor QDSCs matrix have been demonstrated.

Energy is important for the evolution of humans, and human civilization has eternally searched for sustainable energy supply.[1] A milestone invention, the solar cell, allows abundant solar energy to be directly converted into electricity with low carbon emissions and geographical limitations.[1, 2, 3] III–V multi-junction cells and 'flat-plate' silicon technologies are the primary workhorse for photovoltaics (PVs) under varied irradiation conditions including flat panel solar cells, concentration PVs (CPVs), outer space solar panels, and indoor solar cells, which deliver considerable power to our daily life. However, there are several confront challenges need to be addressed, such as higher cost, lower sustainability and flexibility.[4, 5] Compared to most photoactive materials in the emerging 3rd generation PV, colloidal metal chalcogenide quantum dot solar cells (QDSC) are a unique class of photovoltaics (PV) that suffer no compromise between high theoretical efficiency, stability, and low-cost.[6] However, due to their low-performance under simulated sunlight, the development of QDSC is lagging behind other QD technologies such as light-emitting diodes[7] and photodetectors[8].

Lead sulfide (PbS) QDSCs have an excellent ambient tolerance, the broad spectrum for high solar harvesting efficiency, atomic-like energy-level quantization and rough surface nature, which has demonstrated tremendous promise in solar cells (ca. ~13% power conversion efficiency (PCE)),[9-14] as well as the rapid developed infrared PVs.[11, 15] The atomic like quantization that is the presence of discrete energy levels at the valence and conduction bands and the relatively easy way of manipulating the energy of these levels make QD distinctly different materials from all other semiconductors.[16, 17, 18] In particular, above bandgap light excitation of the QD can thus lead to multiexciton generation (MEG) and multi-photon absorption (MPA),[19] where the latter opens opportunities for developing PV technology operating at broad light intensity ranges from very low for indoor applications to very high for concentrated solar technologies.[20, 21] Therefore, focusing on MPA, QDs are fascinating objects for the exploration of new photoconversion avenues since they can offer unique properties or combinations of features, such as active photon-absorption layers.[10, 13, 16, 18, 22]

Herein, we report that PbS QDSCs can efficiently convert photon energies into electricity under a very broad range of light conditions mediated by the MPA process. Ultrafast transient

absorption spectroscopy analysis of the response of PbS QD solid films to various excitation conditions reveal that the strongly coupled QD in the device stack generate a very high density of relatively mobile excitons with interdot hopping times in the range of tens of picoseconds which are also not limited by Auger recombination processes at up to 1.5×10^{19} cm^{-3} exciton densities. In order to demonstrate this capability in functioning devices, we evaluated the performance of QDSCs under indoor and concentrated solar irradiation of over 4 decades of intensities (0.01 to 1000 mW/cm^2) and observed that the devices exhibit a continuous linear increase in short-circuit current density (J_{sc}) and a semi-logarithmic increase in open-circuit voltage (V_{oc}). In addition, we fabricated a polymer lens integrated QD concentration CPV and achieved high PCE 21.29% as well as hundreds of hours of a high irradiance operational stability. For the practical perspective of the QDSCs, we demonstrate that QDSCs can successfully power multiple indoor sensor platforms and have a considerable high-energy conversion performance under simulated, real-world sun insolation. Our work demonstrates that QDs should be considered as a serious option for indoor PVs and low concentration CPVs and highlights areas for a further focus of research activities.

This study is focused on PbS-based QDSCs and their light-matter interactions under various irradiance with a first excitonic peak at approximately 1000 nm (Eg ~1.24 eV). The conventional two-step “synthesis to ligand-exchange” processed ordinary QDSCs (with one Sun PCE of ~9%) were chosen as testbeds, where the device stack QD solid films were formed through soaking ligands (e.g. tetrabutylammonium iodide, TBAI) on a spinning QD film.[9, 23, 24] As shown in the Figure 1a, the optimal ratio of the photo-generated charge carriers by the QDSC to the number of incident photons at a given wavelength (EQE and IQE spectra) well match the spectral window from indoor and solar irradiance, which suggests a rational utilization of the large population of short wavelength photons (e.g., 350 nm to 800 nm) in concentrated or high intensity indoor light can be beneficial for high-performance PV devices.[3, 6, 18, 25] The electron microscopy images (Figure S1) and absorption spectra (Figure S2) of the as-prepared PbS QDs confirm the typical excitonic characteristics of interband optical transitions in a monodispersed, dimensionally confined system.[26]

We used ultrafast transient absorption spectroscopy (TAS), a pump-probe optical spectroscopy method sensitive to photogenerated excitons and charges, to investigate the response of QDSCs under different light conditions (Figure 1b). TAS measurements were carried out with solution and thin film samples of PbS QD with an oleic acid (QD-OA) ligand. Shown in Figure S2, the typical transient absorption spectrum of the samples is dominated by the bleach of the $1S_h$-$1S_e$ absorption. Figure 1C presents the intensity dependent kinetics of the bleach maximum of the film QD-OA and Figure S3 the excitation wavelength dependent

bleach kinetics of the solution QD-OA, which reveal the characteristic for these type of particles picosecond Auger recombination dynamics, a process indicative of MPA or MEG taking place in these systems.[27] TAS experiments were also conducted with ligand-exchanged QD-TBAI solid films (Figure 1c) and a full-stack QDSC (Figure 1d) as a function of light fluence.[28] The results in Figure 1c-1d reveal the disappearance of the picosecond Auger process in these systems (at least in the range of exciton fluences studied 4.1×10^{17}-1.4×10^{19} cm^{-3}) and the appearance of a new and slower relaxation process which we tentatively assign to bimolecular recombination of photogenerated charges. The assignment is based on the low binding energy of excitons in PbS QD[17] and the observation of excitation intensity dependence of the kinetics on the nanosecond timescale which is a typical behaviour for thermally activated charge hopping.[29] The observations of a bleach signal rise seen in Figure 1f and 1g and shifting of the bleach peak maximum seen in Figure S4 are consistent with this picture; they also indicate a thermalization process through a density of trap states and the spatial charge hopping between QDs in the QD-TBAI and full-stack QDSC samples.[17, 30] A likely cause of the suppression of Auger recombination is closer packing and stronger inter-dot coupling in the TBAI-ligand-exchanged QD allowing fast charge escape into neighbouring QD.[31, 32] The suppression of Auger recombination and the slowing down of the charge losses significantly improves the linear response of the active layer to increasing light intensities (Figure 1f), suggesting that devices can principally generate photocurrent linearly above 1 Sun photon flux, provided that charge extraction rates are competitive with the bimolecular recombination losses at J_{sc} and maximum power point (MPP) conditions. It should be noted that the full device stacks exhibited better linear relationship between the excitation fluence and charge generation. We believe the reason could be the energetic gradient created by the multiple layers within the full device stack, where there are layers of QD with different band edge energies,[32] which would enable more effective separation and extraction of charges. It could also be better band bending when packing the QD in the full device stack due to extra material treatment compared to the single QD-TBAI films.[33, 34] Therefore, based on these observations, we focus on investigating the response of QDSCs under varying light circumstances from low density indoor to concentrated over 5 Sun irradiation.[21, 35]

We start our device performance evaluations under short wavelength light irradiance by first recording the QDSC JV curves at light levels equivalent to indoor fluorescent lamps. Figure 2a shows a series of J-V curves obtained under different luminance values (i.e., 200 lux to 2000 lux, Figure S5) that cover most indoor-light levels.[36, 37] An enhancement of J_{sc}, $V_{oc,}$ and the output power density as a function of the input power density can be observed. Consequently, the resulting PCE values from these light sources were up to 19.5%, which are higher than the one Sun world-record performance (~13%).[10, 14] Furthermore, due to the

considerable shunt resistance and ideal factor (Figure S6, Figure S7, Table S1, and Table S2), a proportional increase in the FF was observed as the light density increased. Moreover, as shown in Figure 2b, the unencapsulated QDSC exhibits outstanding 1800 hours stability under the high energy light exposure (Figure S6), which demonstrates the potential of QDSCs for indoor PV applications such as powering the Internet of Things (IoT) or portable electronic devices (PEDs).[37, 38] To demonstrate the viability of QDSCs for indoor-light-sensor network applications, we integrated an IoT circuit consisting of QDSCs and sensors (Figure S8). Figure 2c and Figure 2d show that the QDSCs produce a 19.21 μW power output (i.e., 52.6 mC) and 2.63 V potential and can readily charge the integrated capacitors. As shown in Figure 2e and Figure 2f, our IoT module can be successfully powered by the QDSCs matrix to detect the motion of an object, e.g., a hand, and activated the alarm. Furthermore, we also dynamically tracked the sensing process, which indicates that indoor QDSC modules can continuously power IR motion sensors.

To assess the response of the QDSC at a higher light irradiance, we used QDSCs under simulated concentrated sunlight conditions. In Figure S9-S11, the QDSC efficiency notably increased, and the optimized viable input power density range from our concentrated PV (CPV) simulation system is from 1000 W/m^2 to 5001 W/m^2. As observed from our TAS analysis, the suppression of Auger recombination significantly improves the linear response of the active layer to increasing light intensities (Figure 1f). Therefore, it can be expected that the QDSCs can principally increase their performance with photon flux provided that charge extraction rates are competitive with the bimolecular recombination loss rates. Figure 3a shows the statistics of PCEs for the entire device population under 1-5 Suns concentrations. Indeed, we observe an increase in the PCE with increasing light intensity, which is, however, non-linear. Notably, the PCE reaches a substantial value of 11.6% (Figure 3a inset) at a 1.5 Sun concentration with *ca.* 30% enhancement from just a normal solid-state ligand exchanged QDSC (with one Sun PCE of ~9%). It should be noted that though the main limitation remains the fill factor (FF), the simultaneous enhancement of power output and a stable MPP voltage ratio (0.71±0.02) were observed (Figure S12a), and there is no significant deterioration until intensities above 5 Suns.[36, 39]

At these light irradiance levels, we would expect the FF to increase monotonically with increasing charge-carrier density within the QD film and not reduce with increasing light intensity.[4, 6] We found QDSC PCE (η) evolution arises due to disproportional changes in the J_{sc}, FF and V_{oc} with the photon-flux power input (P_{in}) (Figure S12b, $\eta = \frac{FF \times J_{sc} \times V_{oc}}{P_{in}} \times 100\%$).[6] We note that we did not actively cool the devices during the increasing irradiance tests which may contribute to the V_{oc} and FF deterioration, since V_{oc} drops with increasing temperature.[4,

[40] As described in Figure S13 and Table S4, due to the high cell operation temperature, the parasitic resistance decreases as a function of the solar concentration, which causes the FF to be nonlinear.[41]

One of the potential merit of QDSC is its good ambient tolerance since all the QDSCs are fabricated and at ambient condition without any encapsulation.[9, 10, 33] To access the stability of QDSCs under high irradiance, we measured unencapsulated QDSCs under concentrated sunlight (3 Suns) and list the results in Figure 3b. This light flux was chosen for the stability study because of the high-power output (32.4±0.1 $mWcm^{-2}$) and high PCE (10.8±0.04%) of the QDSC devices. Encouragingly, we observe good stability under the continuous light exposure at 3 Suns, with the cell maintaining 99% of its original efficiency within 10 hours of testing, giving a promise of long term stability of QDSC for outer space panels and low centration CPVs.[25]

To experimentally demonstrate QDSCs are particularly promising for low-concentration CPV applications, we fabricated a solution-processed QD CPV using a polydimethylsiloxane (PDMS) polymer lens with a solar concentration ratio around 3.[41] The ray trajectory simulations determined the 2.3 and 4.08 maximum concentration ratios can be achieved through as-prepared 70° and 140° polymer lenses (Figure 3c, Figure 3d, Figure S14 and Table S5). The lens-integrated module cell current density (MJ) was revealed by the EQE (Figure 3e) and MJ-V curves (Figure 3f). Assuming that the QDSC and polymer lens are integrated (i.e., P_{in}=100 mW/cm^2), these solution-processed QD CPV systems generate a MPD of 21 mW/cm^2, which translates into a considerably high MPCE of 21.29% close to commercialized thin-film PVs.[42] As shown in Figure 3f, a three-fold larger MPCE value can be obtained by covering the QDSC with a 140° polymer lens. These QD CPV systems exhibit promise stability under high-intensity light irradiation, as summarised in Figure S15 and Table S6 presented data from 6 h testing under continuous light exposure. Moreover, we demonstrated conceptual 'water lens' QD CPV systems by manipulating the surface tension of the ITO glass side through forming SAM (self-assembled monolayers) layers. Encouragingly, a significant MPCE and power output can be obtained from this water lens system, which further confirmed the potential and moisture environmental stability of integrated QD CPV systems (Figure S16, Table S7).

In Figure 4a, we summarise the measured J_{SC} and V_{OC} for the unencapsulated devices studied herein under different light intensities. We observe a linear increase in the J_{sc} and a semi-logarithmic increase in the V_{oc} with increasing light intensity (0.01 to 1000 mW/cm^2). The performance of the devices is further analyzed and compared with state-of-the-art PbS QDSCs in Figure 4b and Table S8, where QDSCs are categorized according to the lighting

environments used in the experiments, such as sunlight, indoor and high-intensity light. Besides of the polymer lens integrated QD CPV, the best performance of bared QDSC is under diffused indoor light irradiance, which indicates QDSC may also be suitable for compensating low irradiance in high latitude areas (LA). This effect is shown in Figure 4c, where we report the QDSC efficiency under annual daily irradiance conditions from various LA. We give a full description of our estimations in Table S9 and Figure S17. As highlighted in the periphery of the contour maps (Figure 4c and Figure S18), a remarkable amount of power can be efficiently generated under various light illumination conditions and adequately attuned for the irradiance difference due to LA variations (e.g., high LA regions or dark intervals).[43]

In summary, we have observed excellent performance and good stability of QDSCs under an indoor and concentrated solar irradiance of over 4 decades for irradiance power densities from 0.01 to 1000 mW/cm^2. By investigating the ultrafast exciton dynamics of QDs solids and device stacks, we found that replacement of OA with TBAI ligand suppresses Auger recombination and enhances charge diffusion within the devices. The suppression of Auger recombination and slowing down of charge losses indicated that the photocurrent of the QDSCs can increase simultaneously with photon flux, provided that the charge extraction rates are competitive with the bimolecular recombination losses at short circuit and maximum power point conditions. Based on these findings, we show a 19.5% (2000 lux indoor light), and an 11.6% efficiency (1.5 Suns) can be easily obtained from a very ordinary solid-state ligand exchanged QDSCs (9.55% under 1 Sun). We further achieve a 21.29% efficiency based on polymer lens CPVs and demonstrate viable indoor sensor networks from QDSCs matrix. In the end, we demonstrated unencapsulated QDSC can generate enough power to remedy insufficient irradiance in high LA regions. We expect that the material innovation and fast developments in the research field of metal chalcogenide PVs will realize non-toxic QDSCs in the near future which could enable QD CPV and indoor cells for green energy supply in our daily life.

Experimental Section

Synthesis and purification of PbS and ZnO QDs. We synthesized PbS and ZnO QDs using previously reported methods.[9, 23] All chemicals were purchased from Sigma Aldrich and used without further purification.

Femtosecond transient absorption spectroscopy (fs-TAS) for QD solution and thin films. The as-prepared QDs were precipitated from toluene by adding an excess of acetone, and the mixture was centrifuged at 8,000 rpm for 10 min. After vacuum drying the QDs, they were dispersed in tetrachloroethylene to form a homogeneous, colloidal, stable solution with

absolute infrared transparency. The concentration of the PbS QDs was pre-fixed to an optical density (O.D.) of 0.07 at the first exciton peak. Film QD samples were prepared as follows: Glass/QDs with pristine OA ligand; Glass/QDs with TBAI ligand; ITO/ZnO/QDs with TBAI ligand/QDs with EDT ligand following procedures for device preparation. All films were prepared with 0.25(±0.03) absorbance at their lowest energy excitonic peak maximum.

Fs-TAS analysis was carried out using a HELIOS (Ultrafast Systems) transient absorption spectrometer seeded with 800 nm 100 fs pulses generated at 1 KHz by a Solstice Ti: Sapphire regenerative amplifier (Newport Ltd).[28, 44] A TOPAS (Light conversion) optical parametric amplifier was used to generate the excitation pulses, and their intensity was attenuated using a gradual neutral density filter. Experiments were conducted at a standard temperature and pressure conditions. Solution measurements were carried out using a quartz cuvette with a 2-mm beam path with an inserted magnetic stirrer, while films were measured in a 2 cm quartz cuvette put under constant nitrogen pressure. Degradation was not observed during the experiments. Pump pulse energies were measured with Vega Ophir power meter. Film thicknesses for the calculation of exciton densities used in the TAS experiments were measured using KLA Tencor D-600 profilometer.

Device fabrication. We fabricated a QDSC using a modified version of previously reported methods.[9, 23] ITO substrates were treated with oxygen plasma for 5 min before the device fabrication. ZnO QDs (50 mg/mL) were spin-coated onto ITO substrates at 2,000 rpm for 30 seconds. Then, the ZnO QD solid film was annealed at 250 °C over a period of 30 min and then allowed to cool down to room temperature. The PbS QD solid film was fabricated via a layer-by-layer spin-casting protocol: i) A PbS QD solution (50 mg/mL) was spin cast onto the substrate at 2,000 rpm for 15 seconds. ii) A tetrabutylammonium iodide (TBAI) solution (10 mg/mL in methanol) was drop cast onto the substrate for 30 seconds and spun at 2,000 rpm for 30 seconds to form a QD film. This film was then rinsed twice with methanol before applying a subsequent QD layer (10 layers in total). iii) A 1,2-ethanedithiol (EDT) solution (0.02% volume in acetonitrile) was applied to the substrate via spin casting after the deposition of the PbS QD solution. After washing twice with acetonitrile, the final device was transferred into a thermal evaporator. Au contact pins were thermally evaporated onto the films through shadow masks. The device areas were defined by applying 0.012 cm^2 masks.

Integrated QDSC and sensor circuit fabrication. The demonstration circuit for the sensor application consists of QDSCs (10 cells were connected in series), capacitors (10 ~ 30 mF), a switch, and an IR motion sensor. Commercially available IR motion sensor, capacitors and 2000 lux fluorescent light (Phillips) were used for the demonstration. Equivalent circuit and detail circuit parameters can be found in Figure 2e, Supplementary Figure S8, and Table S3.

Device characterization. Solar cell measurement protocols are provided in Figure S19 and Table S10. These protocols were used for evaluating QDSC performance and stability under sunlight, indoor-light, and high-intensity light irradiance. The AM 1.5G J-*V* curves were recorded using a Keithley 2400 instrument under simulated solar light illumination from a LOT Quantum Design simulator (LSE340/1/850.27C) equipped with 300 W Xe arc lamps. The light intensity was calibrated using a RERA SOLUTIONS silicon reference cell (RQS4695) before each measurement. The ambient low-light (200 lux to 10,000 lux) J-V curves were obtained using a Keithley 2400 source meter under a series of fluorescent lamps with reflectors (Osram L18W/827). The lux levels of the fluorescence lamps were measured by a lux meter (LX-1330B). The light intensity of the fluorescent lamps was calibrated by a Thorlabs PM100D power and energy meter equipped with a Thorlabs S401C high-sensitivity thermal sensor. We employed a series of optical density filters to obtain different light intensities under one Sun illumination. The high-intensity light (1 Sun to 30 Suns) J-V curves were obtained using a Class AAA solar simulator system (WXS-220S-L2, Wacom, KANC, as shown in Figure S7) equipped with a xenon lamp (x1), halogen lamps (x3), Fresnel lens and IR/UV filters to achieve different sun irradiance levels. The effective irradiated area was from 484 cm^2 (1 Sun) to 0.25 cm^2 (500 Suns).

Quantum efficiency (EQE and IQE). A SpeQuest quantum efficiency (QE) system was employed to measure the external quantum efficiency (EQE) and internal quantum efficiency (IQE). The QE system had a 100 W quartz tungsten halogen light and 150 mm F/4.2 monochromator as a photon source and an SR830 DSP lock-in amplifier (locked to light chopped at 83 Hz) and a Melles Griot IV converter to extract the photocurrent. The wavelength range was from 350 nm to 1800 nm, and all the measurement were calibrated using NIST silicon (200 nm-1100 nm) and germanium (700-1800 nm) reference cells with areas pre-defined by a mask (0.012 cm^2). To measure the IQE, the EQE was measured, and then, the reflected signal (light) was excluded. An integrated sphere (Ocean Optics ISP-30-6-R) was employed to measure the reflected signal (direct and diffuse reflections), and a reflectance standard was applied to calibrate the system before each measurement.

Polymer micro-lens fabrication. A polydimethylsiloxane (PDMS) elastomer base (Sylgard 184, Dow Corning) was mixed with the curing agent at a weight ratio of 20:1 and degassed at room temperature for 1 h. Then, 0.02-0.04 mL of the PDMS solution was dropped onto a preheated hot plate with a syringe and allowed to solidify in the temperature range of 200-300 °C for 1 min. The geometrical properties of the PDMS lens were controlled by the heating temperature for a fixed droplet volume and height. For instance, the angles of 70° and 140° with a diameter of 0.5~0.7cm (minimum 0.5 cm) were fabricated at 200°C and 280°C, respectively.

Ray trajectory simulation. Polymer lens concentrator simulations were performed using the Ray Optics module of the COMSOL Multiphysics software suite. As shown in Figure S15, the geometric profiles were interpolated from the two fabricated micro-lenses with contact angles of θ_1=140° and θ_2=70°. In each case, a 100 mW/cm^2 initial flux density (I_{in}) was applied to the lens surface using an illuminated surface boundary condition, and only the refracted rays were evaluated. The number of calculated beams was N=10^5. A rectangular surface, i.e., a focal plane, was placed 1.1 mm away from the lens to match the thickness of the ITO glass. By applying a wall boundary condition, we calculated the incident flux density (I_f) on the active area of the focal plane as A=0.08$\times$0.15 cm^2. The local concentration ratio (R) was evaluated using the equation

$$R = \frac{I_f}{I_{in}}$$

Detailed simulation parameters are listed in Supplementary Table S5.

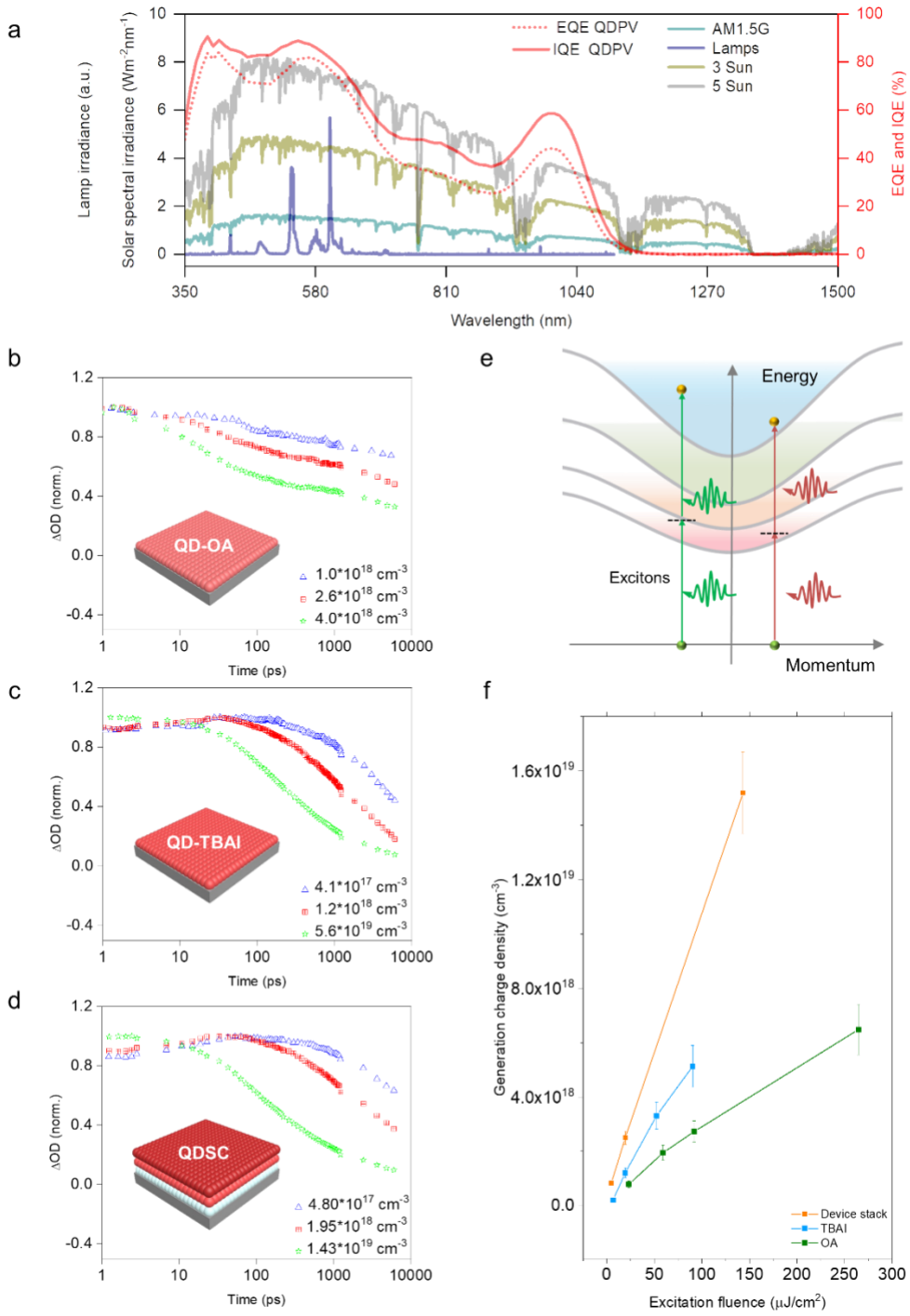

Figure 1| Various light spectra and QD solid film and device MPA ultrafast exciton dynamics. a, The spectra of AM 1.5G and low-concentration (e.g., 3 and 5 Suns) solar irradiance, a fluorescent lamp (1000 lux) and the QE (external and internal) spectra derived from 1.24 eV PbS QDs. Transient absorption kinetics recorded for QD with an oleic acid ligand (b), QD solid thin film with TBAI ligand (c) and full device stack (d), demonstrating the transition from Auger to bimolecular charge recombination losses with ligand exchange. e, Schematic illustrating the MPA process in QD solids. f, Charge densities generated as a function of light fluence, estimated from the lowest energy bleach signal in the transient absorption spectra of the dots and recorded using 526 nm excitation pulse.

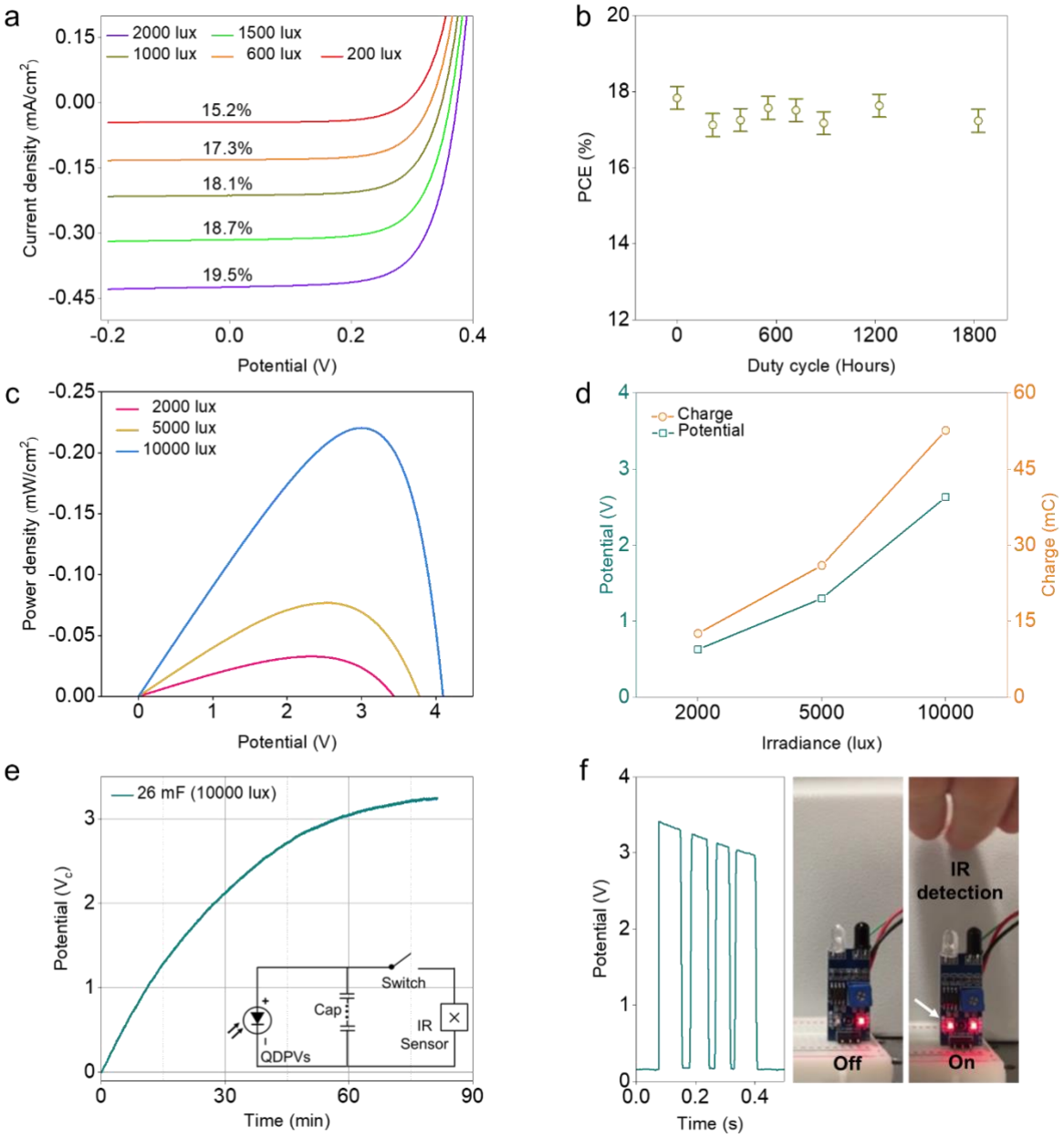

Figure 2| Indoor performance of QDSCs and an integrated IoT sensor module. a, J-V curves and PCE values at different room light irradiance levels. b, The unencapsulated QDSC PCE stability performance under 1000 lux insolation for a continuous 1800 hours exposure. c and d, Power, photovoltage and charge from the integrated QDSC circuits as a function of the ambient indoor irradiance. e, Capacitor charging curve under ambient light; inset describes an integrated circuit of QDSCs, capacitors and an IR sensor. f, Snapshots and transient signals from the IR sensor.

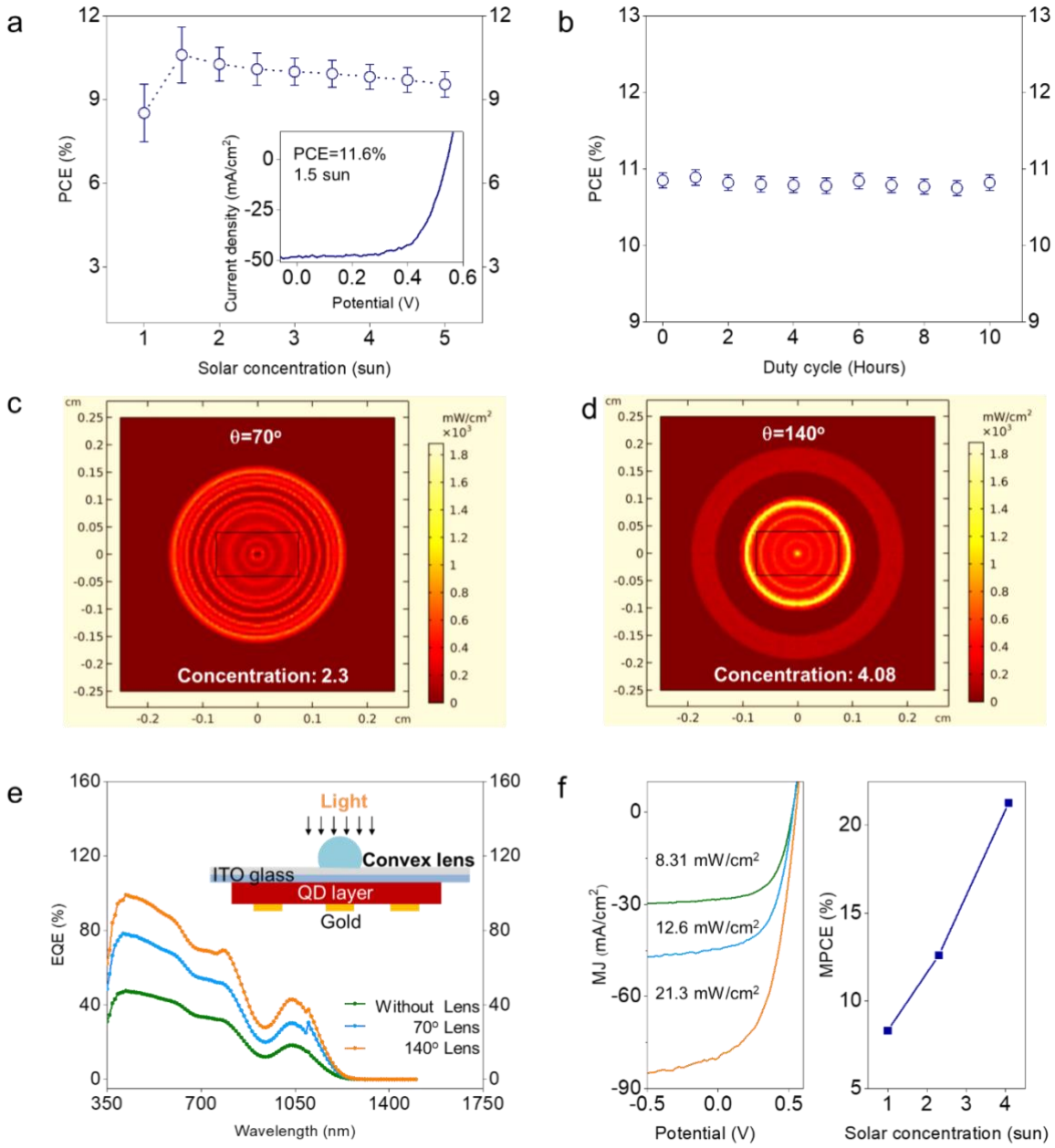

Figure 3| QD CPV system and integrated polymer-lens CPV system characteristics. a, PCE performance of QDSCs under different solar concentrations. The inset displays the J-V curve of the as-prepared champion cell. b, Unencapsulated QDSC PCE stability performance under 3 Suns insolation for a continuous 10 hours exposure. c, d, Ray trajectories simulated with COMSOL Multiphysics emanating from a 70° and 140° contact angle micro-lens. e, EQE curves of the QD polymer-lens CPV system under 1.5G AM irradiance. Inset of (e) shows the structure of the QD CPV system. f, MJ-V, and MPCE as a function of the solar concentration ratio.

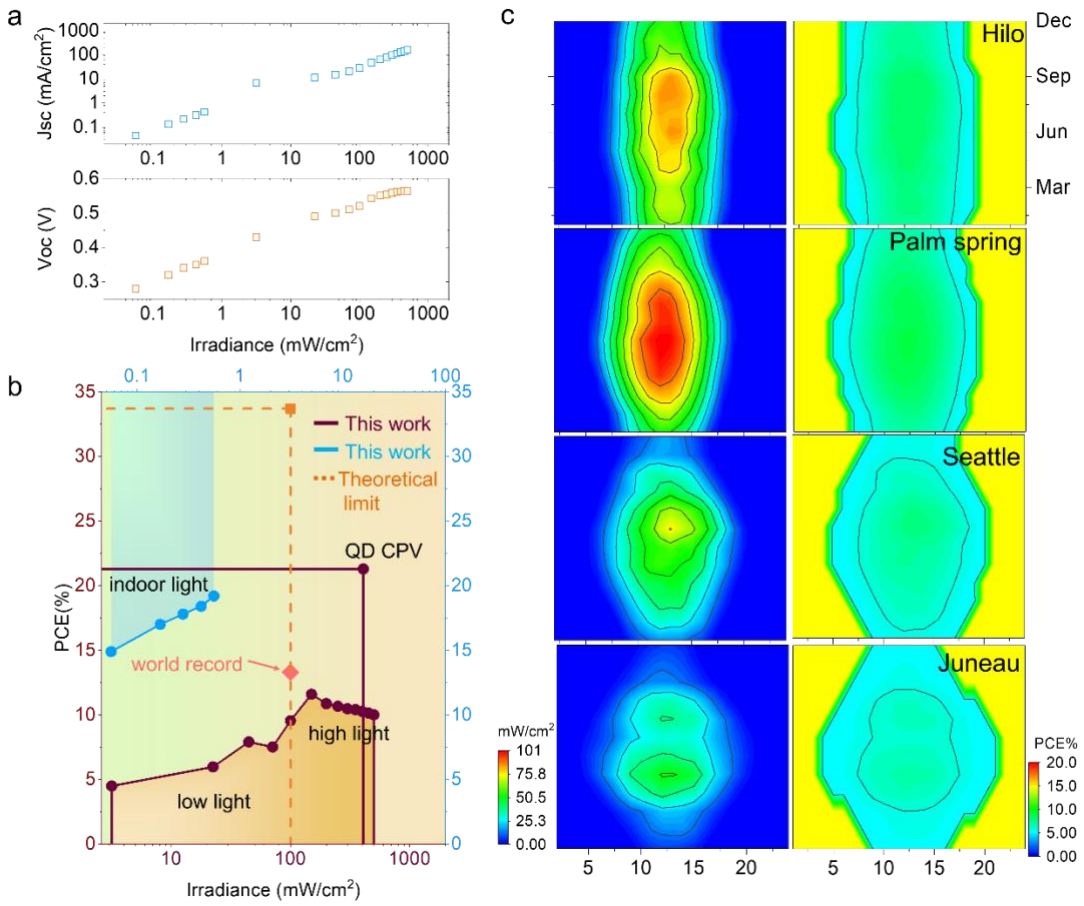

Figure 4| QDSC performance under various lighting conditions. J_{sc}, V_{oc} (a) and PCE (b) evolution under variable ambient (indoor) and solar (sunlight, high-intensity light) irradiance levels. ■ is theoretical limit-based Shockley–Queisser equation and ♦ is the current PbS QDSC world record.[14] The Jsc, irradiances are plotted in logarithm scale, Voc and PEC are plotted in linear scale. c, Left panel shows mean annual daily irradiance of four USA cities among different LA; right panel shows simulated mean annual daily QDSC efficiency from selected cities.

Reference:

[1] S. Chu, Y. Cui, N. Liu, Nat Mater 2017, 16, 16.
[2] M. Freitag, J. Teuscher, Y. Saygili, X. Zhang, F. Giordano, P. Liska, J. Hua, S. M. Zakeeruddin, J.-E. Moser, M. Grätzel, A. Hagfeldt, Nat. Photonics 2017, 11, 372; D. M. Chapin, C. S. Fuller, G. L. Pearson, J. Appl. Phys. 1954, 25, 676.
[3] A. Polman, M. Knight, E. C. Garnett, B. Ehrler, W. C. Sinke, Science 2016, 352.
[4] Z. Wang, Q. Lin, B. Wenger, M. G. Christoforo, Y.-H. Lin, M. T. Klug, M. B. Johnston, L. M. Herz, H. J. Snaith, Nature Energy 2018, 3, 855.
[5] F. Meinardi, S. Ehrenberg, L. Dhamo, F. Carulli, M. Mauri, F. Bruni, R. Simonutti, U. Kortshagen, S. Brovelli, Nat. Photonics 2017, 11, 177; M. Freitag, J. Teuscher, Y. Saygili, X. Zhang, F. Giordano, P. Liska, J. Hua, S. M. Zakeeruddin, J.-E. Moser, M. Grätzel, A. Hagfeldt, Nat. Photonics 2017, 11, 372.
[6] J. Nelson, *The Physics of Solar Cells*, Imperial College Press, 2003.
[7] T.-H. Kim, D.-Y. Chung, J. Ku, I. Song, S. Sul, D.-H. Kim, K.-S. Cho, B. L. Choi, J. Min Kim, S. Hwang, K. Kim, Nat. Commun. 2013, 4, 2637; T.-H. Kim, K.-S. Cho, E. K. Lee, S. J. Lee, J. Chae, J. W. Kim, D. H. Kim, J.-Y. Kwon, G. Amaratunga, S. Y. Lee, B. L. Choi, Y. Kuk, J. M. Kim, K. Kim, Nat. Photonics 2011, 5, 176; K.-S. Cho, E. K. Lee, W.-J. Joo, E. Jang, T.-H. Kim, S. J. Lee, S.-J. Kwon, J. Y. Han, B.-K. Kim, B. L. Choi, J. M. Kim, Nat. Photonics 2009, 3, 341.
[8] V. Adinolfi, E. H. Sargent, Nature 2017, 542, 324.
[9] B. Hou, Y. Cho, B. S. Kim, J. Hong, J. B. Park, S. J. Ahn, J. I. Sohn, S. Cha, J. M. Kim, ACS Energy Lett. 2016, 1, 834.
[10] M. Liu, O. Voznyy, R. Sabatini, F. P. Garcia de Arquer, R. Munir, A. H. Balawi, X. Lan, F. Fan, G. Walters, A. R. Kirmani, S. Hoogland, F. Laquai, A. Amassian, E. H. Sargent, Nat. Mater. 2017, 16, 258.
[11] B. Sun, O. Ouellette, F. P. García de Arquer, O. Voznyy, Y. Kim, M. Wei, A. H. Proppe, M. I. Saidaminov, J. Xu, M. Liu, P. Li, J. Z. Fan, J. W. Jo, H. Tan, F. Tan, S. Hoogland, Z. H. Lu, S. O. Kelley, E. H. Sargent, Nat. Commun. 2018, 9, 4003.
[12] M. J. Speirs, D. N. Dirin, M. Abdu-Aguye, D. M. Balazs, M. V. Kovalenko, M. A. Loi, Energy Environ. Sci. 2016, 9, 2916.
[13] J. Xu, O. Voznyy, M. Liu, A. R. Kirmani, G. Walters, R. Munir, M. Abdelsamie, A. H. Proppe, A. Sarkar, F. P. García de Arquer, M. Wei, B. Sun, M. Liu, O. Ouellette, R. Quintero-Bermudez, J. Li, J. Fan, L. Quan, P. Todorovic, H. Tan, S. Hoogland, S. O. Kelley, M. Stefik, A. Amassian, E. H. Sargent, Nature Nanotechnology 2018.
[14] M.-J. Choi, F. P. García de Arquer, A. H. Proppe, A. Seifitokaldani, J. Choi, J. Kim, S.-W. Baek, M. Liu, B. Sun, M. Biondi, B. Scheffel, G. Walters, D.-H. Nam, J. W. Jo, O. Ouellette, O. Voznyy, S. Hoogland, S. O. Kelley, Y. S. Jung, E. H. Sargent, Nat. Commun. 2020, 11, 103.
[15] S.-W. Baek, S. Jun, B. Kim, A. H. Proppe, O. Ouellette, O. Voznyy, C. Kim, J. Kim, G. Walters, J. H. Song, S. Jeong, H. R. Byun, M. S. Jeong, S. Hoogland, F. P. García de Arquer, S. O. Kelley, J.-Y. Lee, E. H. Sargent, Nature Energy 2019, 4, 969.
[16] A. J. Nozik, Physica E: Low-dimensional Systems and Nanostructures 2002, 14, 115; P. V. Kamat, J. Phys. Chem. Lett. 2013, 4, 908; B. Hou, Israel Journal of Chemistry 2019, 59, 637.
[17] A. H. Proppe, J. Xu, R. P. Sabatini, J. Z. Fan, B. Sun, S. Hoogland, S. O. Kelley, O. Voznyy, E. H. Sargent, Nano Lett. 2018, 18, 7052.
[18] G. H. Carey, A. L. Abdelhady, Z. Ning, S. M. Thon, O. M. Bakr, E. H. Sargent, Chem. Rev. 2015, 115, 12732.
[19] M. T. Trinh, A. J. Houtepen, J. M. Schins, T. Hanrath, J. Piris, W. Knulst, A. P. L. M. Goossens, L. D. A. Siebbeles, Nano Lett. 2008, 8, 1713.
[20] M. C. Beard, J. C. Johnson, J. M. Luther, A. J. Nozik, Philos. Trans. Royal Soc. A 2015, 373, 20140412; N. S. Makarov, P. C. Lau, C. Olson, K. A. Velizhanin, K. M. Solntsev, K. Kieu, S. Kilina, S. Tretiak, R. A. Norwood, N. Peyghambarian, J. W. Perry, ACS Nano 2014, 8, 12572; C. M. Cirloganu, L. A. Padilha, Q. Lin, N. S. Makarov, K. A. Velizhanin, H.

Luo, I. Robel, J. M. Pietryga, V. I. Klimov, Nat. Commun. 2014, 5, 4148; G. Nair, L.-Y. Chang, S. M. Geyer, M. G. Bawendi, Nano Lett. 2011, 11, 2145; R. D. Schaller, V. I. Klimov, Phys. Rev. Lett. 2004, 92, 186601; R. G. Ispasoiu, Y. Jin, J. Lee, F. Papadimitrakopoulos, T. Goodson, Nano Lett. 2002, 2, 127.
[21] L. A. Padilha, G. Nootz, P. D. Olszak, S. Webster, D. J. Hagan, E. W. Van Stryland, L. Levina, V. Sukhovatkin, L. Brzozowski, E. H. Sargent, Nano Lett. 2011, 11, 1227.
[22] F. Meinardi, S. Ehrenberg, L. Dhamo, F. Carulli, M. Mauri, F. Bruni, R. Simonutti, U. Kortshagen, S. Brovelli, Nat Photon 2017, 11, 177; Y. Yan, R. W. Crisp, J. Gu, B. D. Chernomordik, G. F. Pach, Ashley R. Marshall, J. A. Turner, M. C. Beard, Nature Energy 2017, 2, 17052.
[23] B. Hou, Y. Cho, B.-S. Kim, D. Ahn, S. Lee, J. B. Park, Y.-W. Lee, J. Hong, H. Im, S. M. Morris, J. I. Sohn, S. Cha, J. M. Kim, J. Mater. Chem. C 2017, 5, 3692.
[24] Y. Wang, Z. Liu, N. Huo, F. Li, M. Gu, X. Ling, Y. Zhang, K. Lu, L. Han, H. Fang, A. G. Shulga, Y. Xue, S. Zhou, F. Yang, X. Tang, J. Zheng, M. Antonietta Loi, G. Konstantatos, W. Ma, Nat. Commun. 2019, 10, 5136.
[25] M. A. Green, S. P. Bremner, Nat Mater 2017, 16, 23.
[26] M. C. Beard, J. M. Luther, O. E. Semonin, A. J. Nozik, Acc. Chem. Res. 2013, 46, 1252; I. Kang, F. W. Wise, J. Opt. Soc. Am. B 1997, 14, 1632.
[27] R. J. Ellingson, M. C. Beard, J. C. Johnson, P. Yu, O. I. Micic, A. J. Nozik, A. Shabaev, A. L. Efros, Nano Lett. 2005, 5, 865.
[28] S. D. Dimitrov, M. Azzouzi, J. Wu, J. Yao, Y. Dong, P. S. Tuladhar, B. C. Schroeder, E. R. Bittner, I. McCulloch, J. Nelson, J. R. Durrant, J. Am. Chem. Soc. 2019, 141, 4634; S. D. Dimitrov, S. Wheeler, D. Niedzialek, B. C. Schroeder, H. Utzat, J. M. Frost, J. Yao, A. Gillett, P. S. Tuladhar, I. McCulloch, J. Nelson, J. R. Durrant, Nat. Commun. 2015, 6, 6501.
[29] J. Nelson, Phys. Rev. B 2003, 67, 155209.
[30] R. H. Gilmore, E. M. Y. Lee, M. C. Weidman, A. P. Willard, W. A. Tisdale, Nano Lett. 2017, 17, 893.
[31] B.-S. Kim, J. Hong, B. Hou, Y. Cho, J. I. Sohn, S. Cha, J. M. Kim, Appl. Phys. Lett. 2016, 109, 063901; D. Bederak, D. M. Balazs, N. V. Sukharevska, A. G. Shulga, M. Abdu-Aguye, D. N. Dirin, M. V. Kovalenko, M. A. Loi, ACS Applied Nano Materials 2018, 1, 6882.
[32] B. Kundu, A. J. Pal, J. Phys. Chem. C 2018, 122, 11570.
[33] C.-H. M. Chuang, P. R. Brown, V. Bulović, M. G. Bawendi, Nat. Mater. 2014, 13, 796.
[34] B. Hou, Y. Cho, B. S. Kim, J. Hong, J. B. Park, S. J. Ahn, J. I. Sohn, S. Cha, J. M. Kim, ACS Energy Lett. 2016, 1, 834.
[35] M. E. Schmidt, S. A. Blanton, M. A. Hines, P. Guyot-Sionnest, Phys. Rev. B 1996, 53, 12629.
[36] H. K. H. Lee, Z. Li, J. R. Durrant, W. C. Tsoi, Appl. Phys. Lett. 2016, 108, 253301.
[37] A. Nasiri, S. A. Zabalawi, G. Mandic, IEEE Trans. Ind. Electron. 2009, 56, 4502.
[38] J. W. Matiko, N. J. Grabham, S. P. Beeby, M. J. Tudor, Meas. Sci. Technol. 2014, 25, 012002.
[39] M. A. Husain, A. Tariq, S. Hameed, M. S. B. Arif, A. Jain, Green Energy Environ. 2017, 2, 5.
[40] M. T. Hörantner, H. J. Snaith, Energy Environ. Sci. 2017, 10, 1983.
[41] S. Ekgasit, N. Kaewmanee, P. Jangtawee, C. Thammacharoen, M. Donphoongpri, ACS Appl. Mater. Interfaces 2016, 8, 20474.
[42] M. A. Green, Y. Hishikawa, W. Warta, E. D. Dunlop, D. H. Levi, J. Hohl-Ebinger, A. W. H. Ho-Baillie, Prog Photovolt Res Appl. 2017, 25, 668.
[43] A. Sacco, M. Gerosa, S. Bianco, L. Mercatelli, R. Fontana, L. Pezzati, M. Quaglio, C. F. Pirri, A. O. M. Tucci, Solar Energy 2016, 125, 307.
[44] S. D. Dimitrov, Z. Huang, F. Deledalle, C. B. Nielsen, B. C. Schroeder, R. S. Ashraf, S. Shoaee, I. McCulloch, J. R. Durrant, Energy Environ. Sci. 2014, 7, 1037.

Keywords:

PbS quantum dots, indoor solar cells, concentration photovoltaic (CPV), multi-photon absorption (MPA), ultrafast transient absorption spectroscopy (TAS)

Author contributions

B.H. and S.C. conceived the experiments and led the project. B.H. and B.S.K. performed material synthesis, device fabrication, and characterization. K.H.L., W.C.T., and Z.L. performed the indoor PV characterization and analysis. S.D. and M.D. conducted the fs-TAS analysis. Y.C. and P.G. performed the circuit construction and ray trajectories simulation. J.D. and J.K. contributed to scientific discussion and provided experimental guidance. M.X.L., J.Z., S.D., and J.S. contributed to the interpretation of the data and commented on the manuscript. B.H. S.D. and S.C. wrote the paper with input and discussion from all authors.

Acknowledgements

We acknowledge funds from National Research Foundation (NRF) of Korea (2019R1A2C1005930), the Engineering and Physical Sciences Research Council (EPSRC, EP/P027628/1) and European Commission Horizon 2020 (685758). Also, the authors would like to thank the Sêr Solar initiative and the European regional development fund through the Welsh government. S.D. would like to thank Amirah Way for support with experiments. B.H. would like to acknowledge the financial support by the Cardiff University as well as EPSRC (EP/K040375/1) for funding the 'South of England Analytical Electron Microscope' used in this research.

Supplementary Materials

Multiphoton Absorption Stimulated Metal Chalcogenide Quantum Dot Solar Cells Under Ambient and Concentrated Irradiance

Bo Hou[1,‡], Byung-Sung Kim[2,‡], Harrison K. H. Lee[3], Yuljae Cho[4], Paul Giraud[2], Mengxia Liu[5,§], Jingchao Zhang[6], Matthew L. Davies[3], James R. Durrant[3,7], Wing C. Tsoi[3], Zhe Li[8], Stoichko Dimitrov[9*], Jung Inn Sohn[10*], SeungNam Cha[11*] and Jong Min Kim[12]

1. Department of Physics and Astronomy, Cardiff University, Cardiff CF24 3AA, United Kingdom
2. Department of Engineering Science, University of Oxford, OX1 3PJ, Oxford, United Kingdom
3. SPECIFIC, College of Engineering, Swansea University, SA1 8EN, Swansea, United Kingdom
4. University of Michigan-Shanghai Jiao Tong University Joint Institute, Shanghai Jiao Tong University, 800 Dong Chuan Road, Minhang District, Shanghai 200240, China
5. Department of Electrical and Computer Engineering, University of Toronto, 10 King's College Road, Toronto, Ontario M5S 3G4, Canada
6. Department of Biostatistics and Bioinformatics, Emory University, Atlanta, GA, 30322, USA
7. Department of Chemistry, Imperial College London, SW7 2AZ, London, United Kingdom
8. School of Engineering and Materials Science (SEMS), Queen Mary University of London, E1 4NS, London, United Kingdom
9. School of Biological and Chemical Sciences, Queen Mary University of London, E1 4NS, London, United Kingdom
10. Division of Physics and Semiconductor Science, Dongguk University, Seoul 100-715, Republic of Korea
11. Department of Physics, Sungkyunkwan University, Suwon, 16419, Republic of Korea
12. Department of Engineering, University of Cambridge, CB3 0FA, Cambridge, United Kingdom

Corresponding authors:
Email: s.dimitrov@qmul.ac.uk
Email: junginn.sohn@dongguk.edu
Email: chasn@skku.edu
‡ These authors contributed equally to this work.
§ Present address: Cavendish Laboratory, University of Cambridge, J. J. Thomson Avenue, Cambridge, CB3 0HE, United Kingdom

Supplementary Contents:

SI. Microscopy analysis

The highly monodispersed feature of as-prepared PbS QDs is demonstrated from the bright-field transmission electron microscopy (BFTEM) on a JEOL JEM-3000F field emission gun TEM at 300 KV. The size of these particles is 2.8 ± 0.2 nm (Figure S1a). The specific cubic nature is evidenced by the cross-grating pattern that was captured by high-resolution BFTEM through [001] zone axis (Figure S1b).[1] These patterns are formed by the 45-degree crossing of the {200} and {220} planes, from which the lattice constant *a* can be directly extracted as 6.0±0.1 Å.[2]

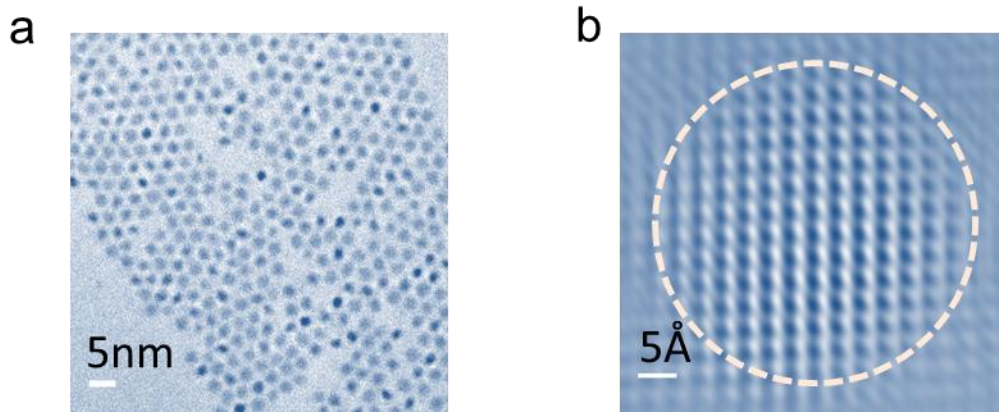

Figure S1. a, b) Bright-field TEM and atomic-scale HRTEM images of as-prepared PbS QDs.

SII. fs-Transient absorption analysis (fs-TAS)

The excitation fluence was estimated by recording the excitation pulse energy through fixed-size arises with a pyroelectric energy sensor (Ophir Photonics PE9). The charge densities in Figure 1g are calculated by dividing the maximum of the transient absorption bleach signal by the number of photons absorbed by the sample and the film thickness measured using a DektakXT.

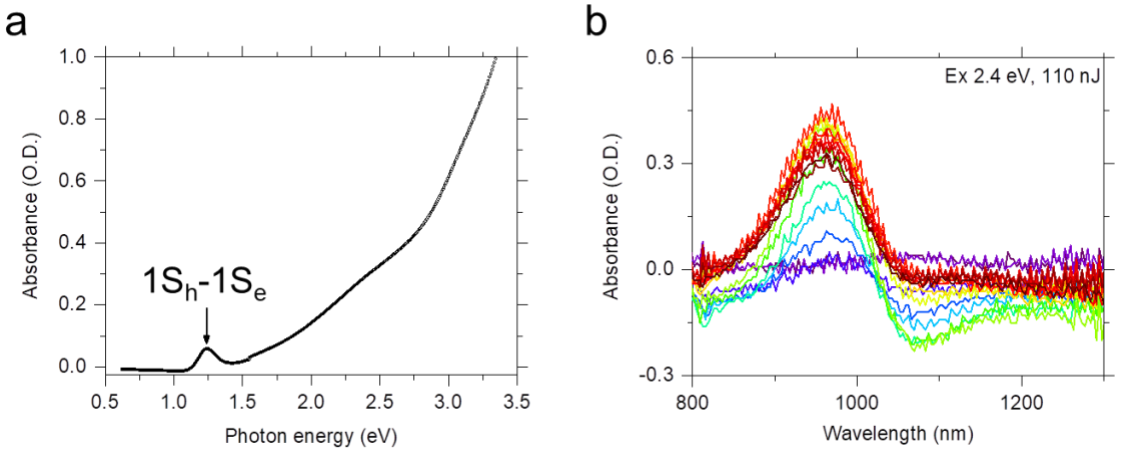

Figure S2. (a) Stationary absorption spectra of as-prepared PbS QDs. (b) Representative transient absorption spectra of PbS nanocrystals for a 2.4 eV excitation from 0.01 (purple&blue) to 6.5 nanoseconds (red&brown). All spectra recorded for different excitation intensities and wavelengths studied in this work showed similar spectral signatures and overall dynamics.

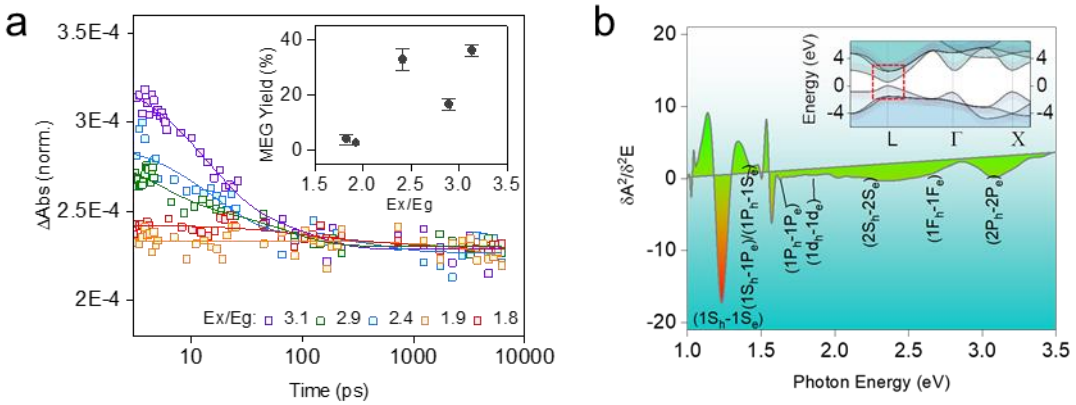

Figure S3. a, Exciton population decay dynamics recorded with different pump photon energies for the QD oleic acid solution demonstrating the presence of multi-exciton generation (MEG) in this sample. This is concluded from the appearance of picosecond Auger signal relaxation at Ex/Eg > 2, where Ex/Eg is the ratio of the excitation photon energy and QD's optical bandgap. The kinetics were recorded at excitation intensities that generated the same exciton fluences in the films. The solid lines are exponential fits to the data. The MEG yields were estimated from the ratio of the amplitude of the TA signal at 3.5 ps (when MEG is complete for all kinetics) and after 160 ps (when the Auger recombination process is complete and only single-exciton relaxation occurs).[3] The inset shows the MEG quantum yields as a function of Ex/Eg. The error bars correspond to the standard deviation of the transient absorption signal noise calculated from the residual of the exponential fits and the pump-energy measurements. b, Interband transition and excitonic peaks of 2.8 nm PbS QDs calculated based on the second derivative of its absorption spectrum. The inset of (b) shows a schematic representation of the DFT calculated the relativistic electronic-band structure of PbS QDs based on k·p perturbation theory.[3-5]

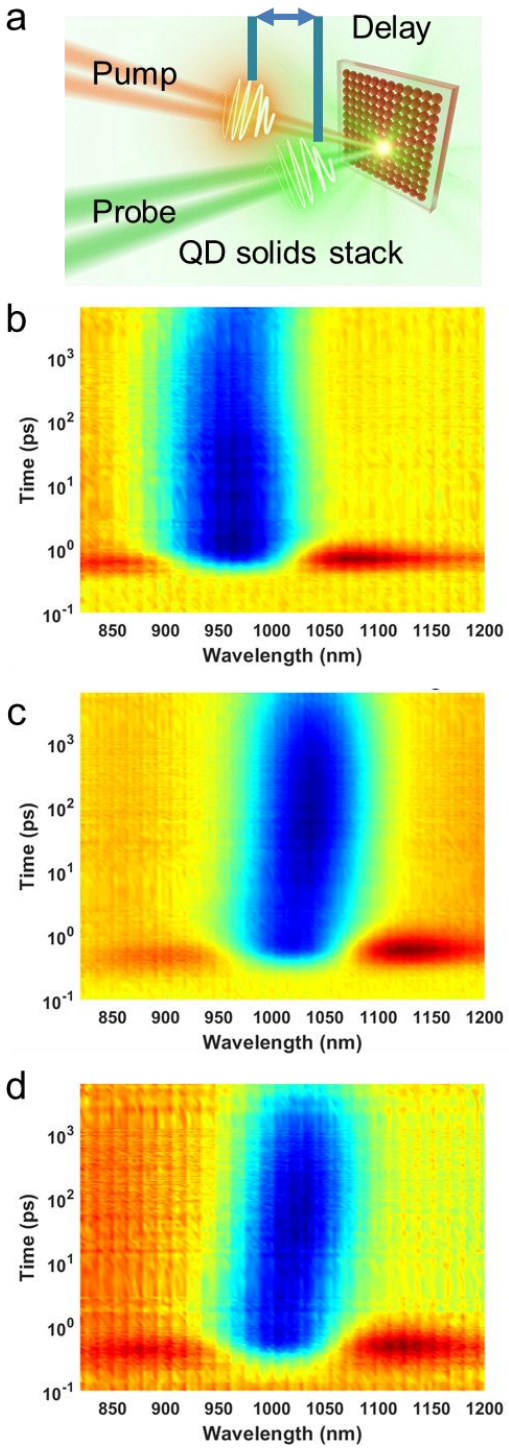

Figure S4. (a) A schematic for employing TAS to investigate the MPA process in solid QD films and devices. 3D $1S_e$-$1S_h$ bleach dynamics of films of (b) PbS-oleic acid (23.4 µJ.cm^{-2}), (c) PbS-TBAI (6.4 µJ.cm^{-2}) and (d) full devices (4.8 µJ.cm^{-2}), recorded using transient absorption spectroscopy and an excitation wavelength of 526 nm. Peak shift for PbS-TBAI and full device result from charge thermalization through the density of states and indicate diffusion of charges through the films. Least square fitting of the peak shift of PbS-TBAI and full device with an exponential function gives 6.8 (±1.1) ps and 15.7 (±3.2) ps for thermalization process, while exponential fitting of the signal rise time gives 14.2 (±0.6) ps and 19.5 (±2.6) ps, respectively. The peak shift energy was calculated to be 21.9 meV (±0.9 meV) for PbS-TBAI film and 20.6 meV (±0.7 meV) for full devices, likely representative of the size dispersity of the prepared films.

SIII Indoor QDSC parameters

Representative indoor lamp spectra with 200 lux and 1000 lux illumination intensity are shown in Figure S5a, b respectively. There is a noticeable lumen counts enrichment (e.g., Figure S5b) can be observed when the illumination altered from 200 lux to 1000 lux. The indoor photostability was evaluated by exposing the QDSC under 1000 lux for 1824 hours. As shown in Figure S6 a-d, there is no noticeable device degradation can be detected. Moreover, a high photon flux induces a smaller shunt and series resistance was observed as illustrated in Figure S6 e-f. Detail QDSC indoor light-harvesting performance parameters are listed in Table S1.

The ideality factor of a diode, *n*, can be extracted from the light intensity dependent and dark diode curves.[6] The extracted plots and values of *n* are listed in Figure S7 and Table S2. The values of *n* usually vary between 1 and 2 depending on charge carrier dynamics. For instance, the *n* equals to 2 when the recombination current dominates, and *n* equals to 1 when the diffusion current dominates. When both currents are comparable, *n* has a value between 1 and 2.[7] Furthermore, we also note that analysis using different evaluating methods may yield slightly different ideality factor values, particularly in the case of under dark or light illumination.[8,9]

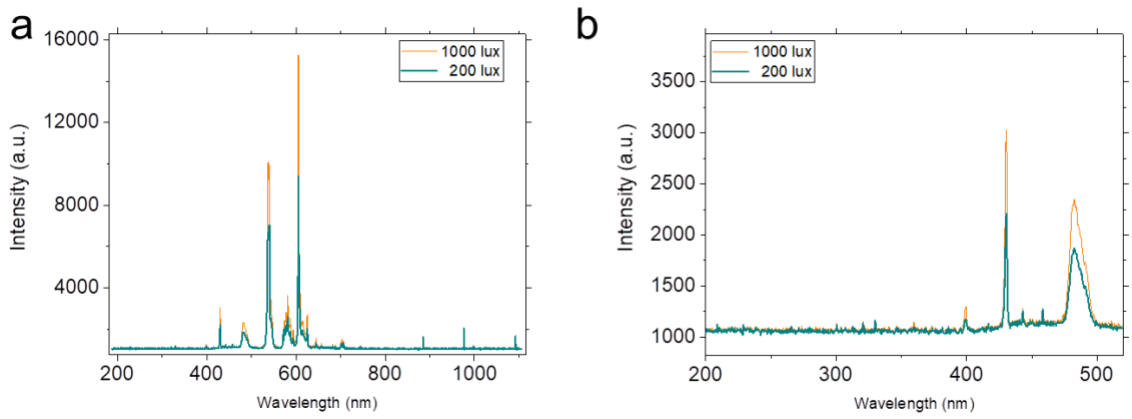

Figure S5. a) The spectra of the indoor lamp with 200 lux and 1000 lux illumination. b) An enlarged view of spectra with photon energy ranging from 200 nm to 520 nm.

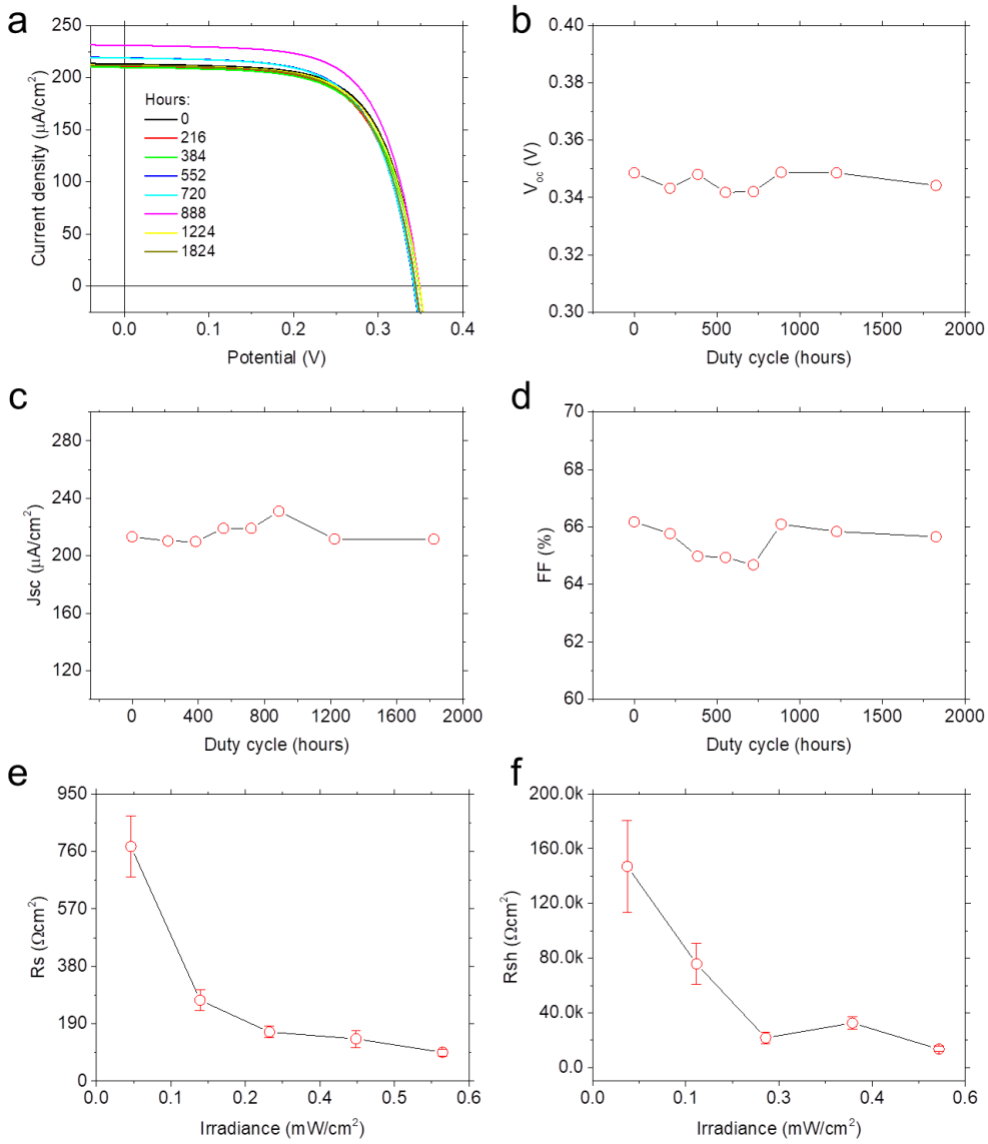

Figure S6. a) J-V curves of QDSC during 1824 hours 1000 lux indoor light exposure. V_{oc} b), J_{sc} c), FF d) evolution as a function of exposure time. e) and f) illustrate the evolution trend of R_s and R_{sh} as a function of irradiance respectively.

Table S1 Summary of indoor QD photovoltaic parameters					
	200 Lux ($0.0557\ mWcm^{-2}$)	600 Lux ($0.1672\ mWcm^{-2}$)	1000 Lux ($0.2787mWcm^{-2}$)	1500 Lux ($0.4181mWcm^{-2}$)	2000 Lux ($0.5574mWcm^{-2}$)
power conversion efficiency (*PCE*)	14.9±0.3% (15.2)	17.0±0.3% (17.3)	17.8±0.3% (18.1)	18.4±0.3% (18.7)	19.2±0.3% (19.5)
fill factor (*FF*)	66.2%	67.6%	69.0%	69.0%	69.4%
ideality factor (*n*)	1.36	1.36	1.36	1.36	1.36
short circuit current density (J_{sc})	$44.6\ \mu A/cm^2$	$130.9\ \mu A/cm^2$	$213.3\ \mu A/cm^2$	$315.3\ \mu A/cm^2$	$423.8\ \mu A/cm^2$
open circuit voltage (V_{oc})	0.28 V	0.32 V	0.34 V	0.35 V	0.36 V
series resistance (R_s)	$776.3\ \Omega cm^2$	$267.6\ \Omega cm^2$	$162.9\ \Omega cm^2$	$139.9\ \Omega cm^2$	$95.5\ \Omega cm^2$
shunt resistance (R_{sh})	$147051.9\ \Omega cm^2$	$75777.7\ \Omega cm^2$	$21696.5\ \Omega cm^2$	$32584.9\ \Omega cm^2$	$13491.4\ \Omega cm^2$

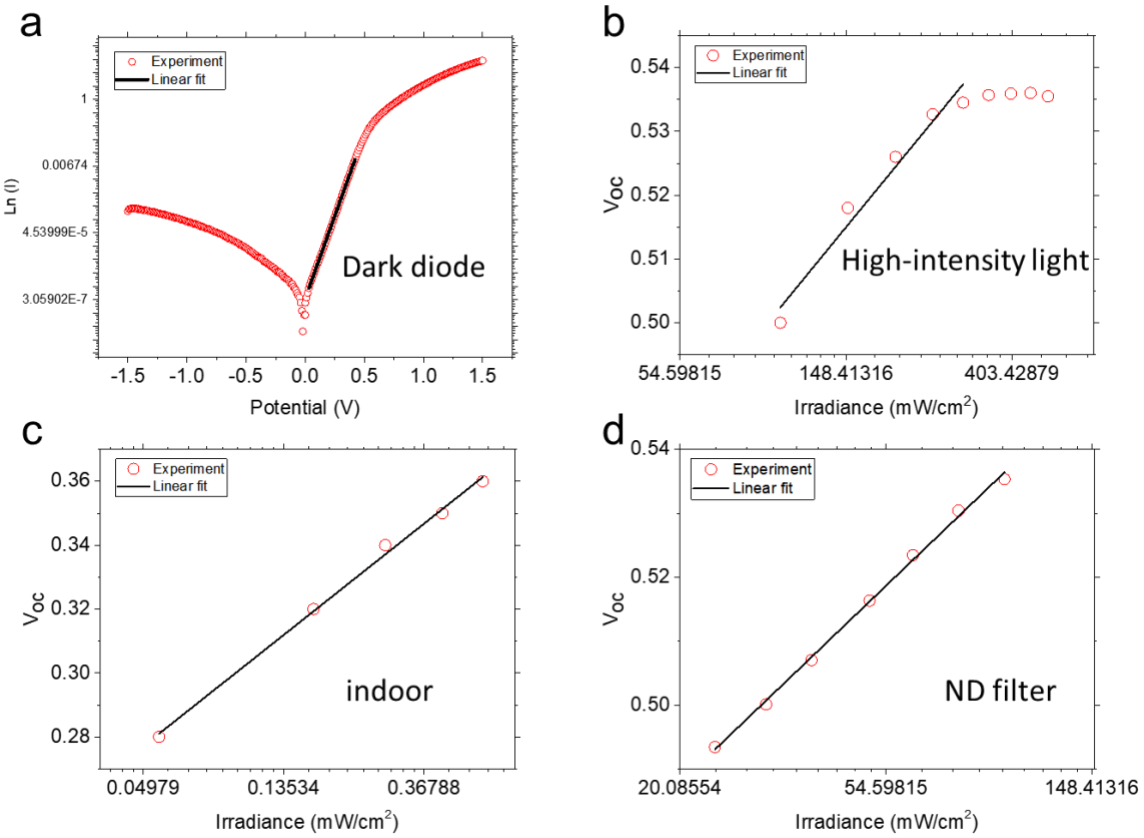

Figure S7. Plots for extraction the n factors such as semi-log dark diode curve a), different irradiance from high-intensity light b), various irradiance from ambient indoor light c), and different one Sun light intensity by employing ND filter d).

Table S2 Summary of ideality factor calculated from different conditions				
calculation condition	High-intensity light	Dark diode	Indoor low light	ND filter
ideality factor (*n*)	1.24	0.96	1.36	1.2

SIV Indoor PV and IR sensor IoT circuit design and parameters

Figure S8a describes the distance-dependent irradiance variation measurement results. It illustrates the feasibility of closely integrating QDSC with indoor illumination system to power sensors. J-V curves and QDSC-Sensor integration circuit design are shown in Figure S8b and c. By closely attach the QDSC with the indoor light system (e.g., Philips fluorescent light), an IR motion sensor can be sufficiently powered. Detail power, potential, and capacitance generation parameters during 1 hour indoor light illumination are listed in Table S3.

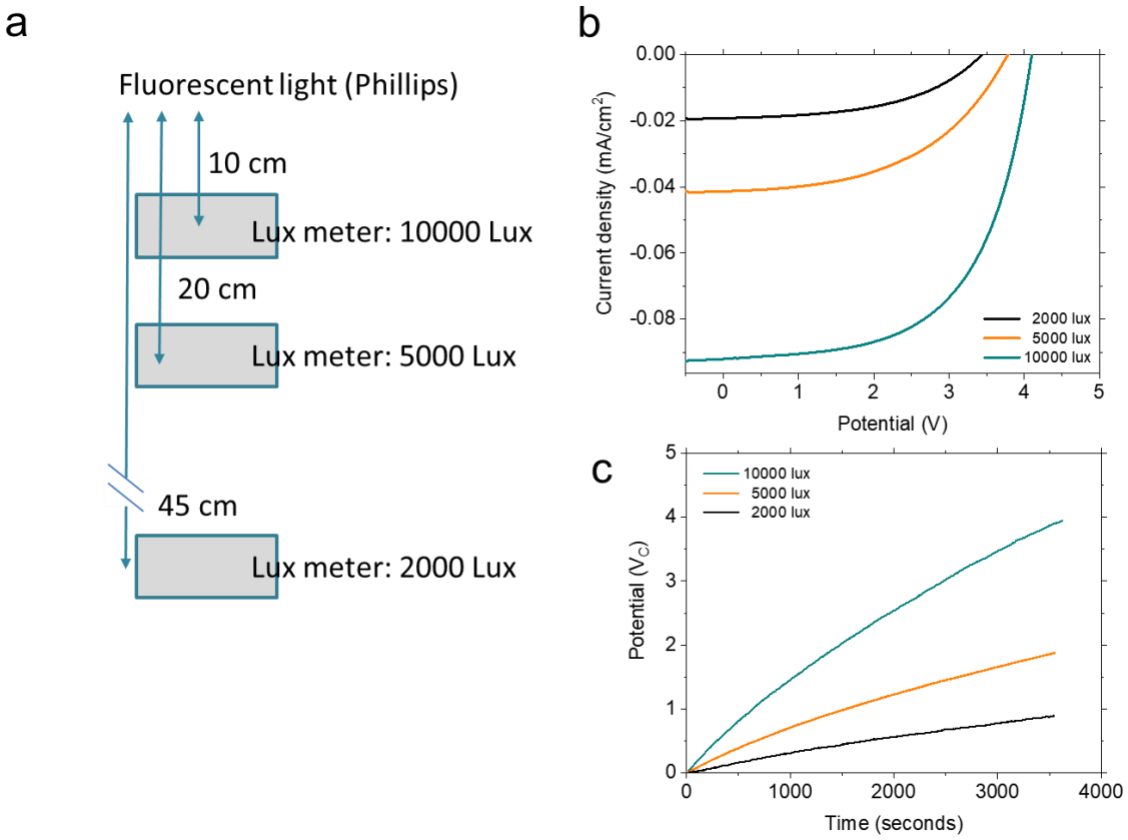

Figure S8. a) The distance-dependent irradiance variation. It should be noted that we simulate the indoor experiment as close as the usual ambient lighting conditions in an office.[6] Because we only focus on obtaining the targeting flux number (such as 2000 lux), therefore, all the lights in the office are switched on. The distance-dependent irradiance variation looks like linear, which is because of the contribution from different light sources. b) J-V curve of QDSC under different indoor irradiance. c) Real-time potential measurement in capacitors (20 mF) which was charged by QDSC under different indoor irradiance.

Table S3 One hour indoor QDSC charging parameters					
Light Intensity [Lux]	Capacitance [mF]	Potential [V]	Q [mC]	Energy [mJ]	Power [uW]
2000	10	1.36	13.6	9.25	2.57
	20	0.63	12.6	6.30	1.75
	30	0.48	14.4	3.46	0.96
5000	10	2.35	23.5	27.61	7.67
	20	1.3	26	16.90	4.69
	30	0.74	22.2	8.21	2.28
10000	10	3.68	36.8	67.71	18.81
	20	2.63	52.6	69.17	19.21
	30	1.47	44.1	32.41	9.00

SV High light QDSC parameters.

The QDSCs were evaluated by high standard AAA class solar simulator system (Figure S9) under a solar concentration from 1 Sun to 30 Suns.

Due to the elevated surface temperature, a noticeable efficiency drop can be observed as shown in Figure S10a (sample A and sample B). Therefore, a low concentration condition (i.e., 1-5 Suns) as highlighted in Figure S10a was employed in the rest of our manuscript. Figure S10b exhibit the general efficiency trend of QDSCs (sample 1 to sample 18) under the solar concentration of 1 to 5 Suns. All the samples showed only small efficiency drop when the solar concentration was increased. Figure S10c and Figure S10d provide more evidence of efficiency evolution trend as a function of solar concentration with multiple time measurements. It indicates that QDSC can sustain a high solar irradiance without noticeable efficiency degradation.

In the range of 1 to 5 Suns, the power conversion efficiency can also be enhanced due to the enrichment of photon flux. As the integration results are shown in the Figure S11a, the number of photons with a wavelength between 280 nm to 500 nm can be dramatically enriched when the solar concentration adjusts from 1 Sun to 5 Suns. The detail J-V and power output curves are provided in Figure S11b, Figure S11c, and Figure S11d.

The power output and maximum power point (MPP) voltage ratio (e.g., essential parameters for evaluating commercial PV products) are extracted and reported in Figure S12a.[6,10] We determined the 'constant MPP ratio' from our QDPV based on a fractional-voltage methodology which was reported to be an effective way for prospecting PV under viable light modulation.[6,11] Solar cell power conversion efficiency (η) is calculated from equation $\eta = \frac{FF \times J_{sc} \times V_{oc}}{P_{in}} \times 100\%$, where J_{sc} denotes short-circuit current density, FF denotes fill factor, V_{oc} denotes open circuit voltage and P_{in} denotes photon flux power input.[12] In practice, without a perfect cell cooling system, the increasing carrier densities and illumination flux will lead to a high dark current density and high cell temperature which inevitably result in the decline of photo conductivity.[12,13] Therefore, though the J_{sc} displays a proportional enlargement, the FF is showing a fast accession, saturation and degeneration trend which subsequently cause deviation of a linear efficiency enhancement (Figure S12b).[12]

By using a differential resistance approach, the series resistance and shunt resistance of QDSC under different irradiance can also be extracted (Figure S13).[2] There is a noticeable decline trend in the parasitic cell resistance, and it is slowing down in the high solar concentration ratio. Moreover, a high photon flux induces a smaller shunt and series resistance was observed which is consistent with the results extracted from indoor light QDSC

as shown in Figure S6 e-f. The parameters of QDSC under different solar concentration, including power conversion efficiency, fill factor, ideality factor, short circuit current density, open circuit voltage, series resistance, shunt resistance are summarised in the Table S4.

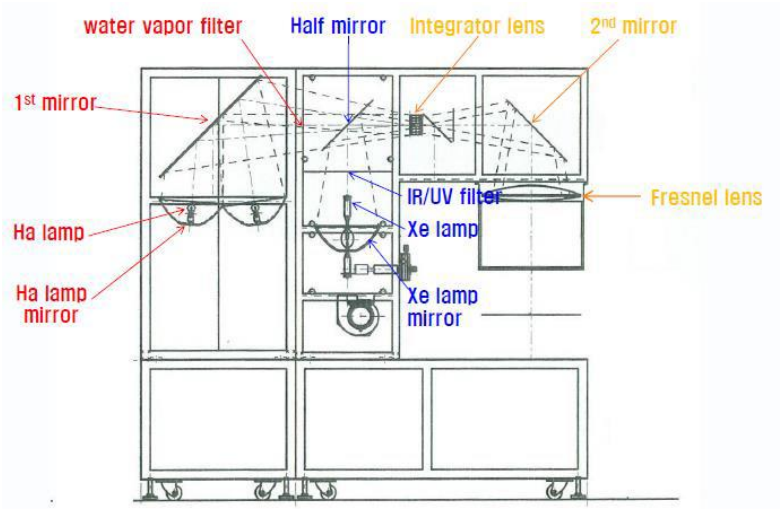

Figure S9. A chart of the concentrated solar simulator system.

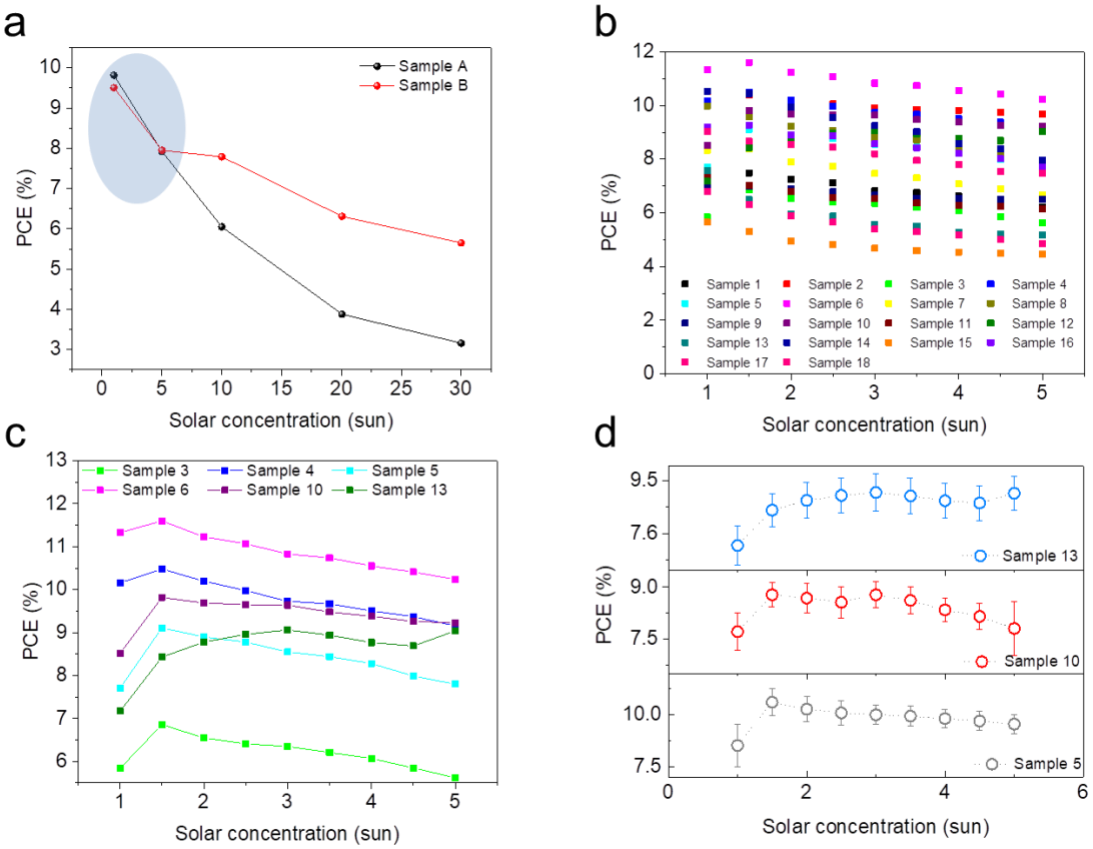

Figure S10. QDSC PCE evolution as a function of solar concentration a) 1~30 Suns, b) 1~5 Suns. Ellipsoidal shade area highlighted the concentration of interest- 1 to 5 Suns low concentration region. c, d) Additional selected QDSC PCE evolutions as a function of solar concentration 1~5 Suns. The error bar in (d) was generated from multiple measurements.

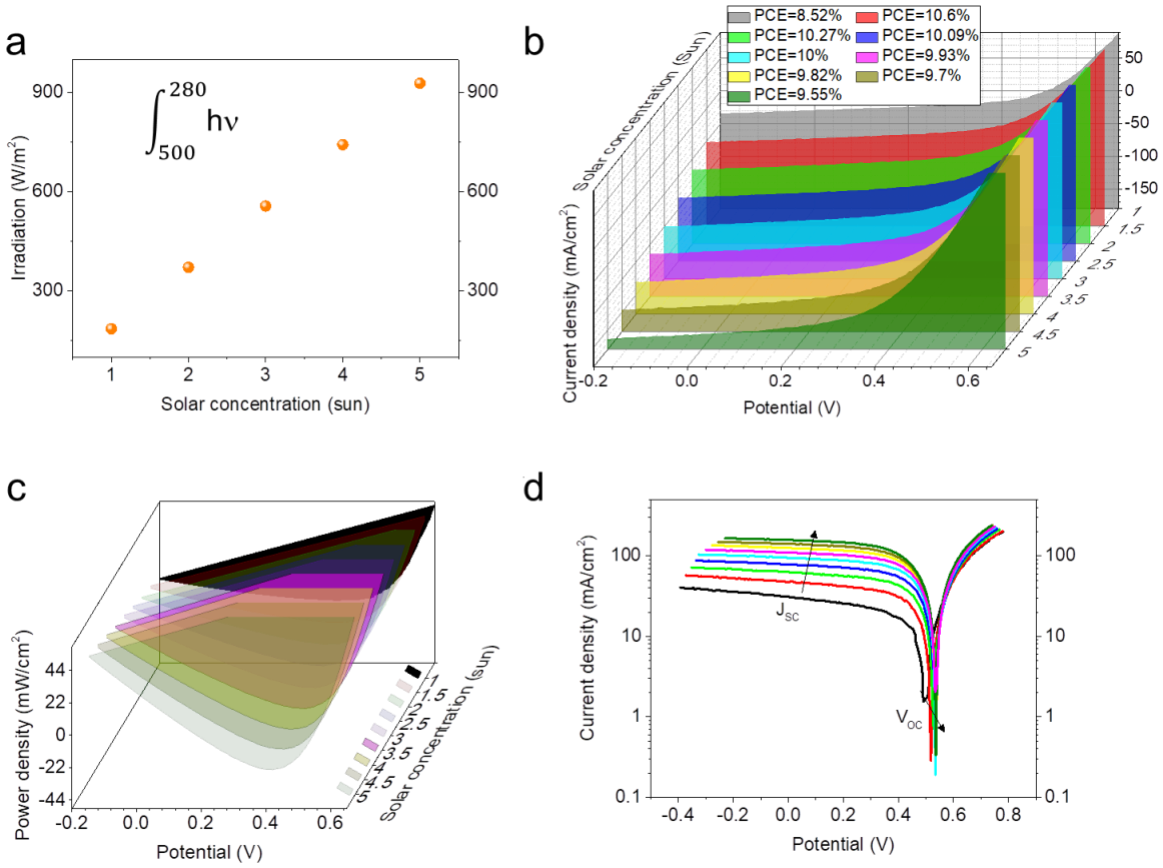

Figure S11. a) Integration of total irradiance between photon wavelengths of 280 to 500 nm. b) J-V curves of a typical QDSC under different solar concentration. c) The power density of QDSC under different solar concentration. d) Semi-log J-V plots of QDSC under different solar concentration.

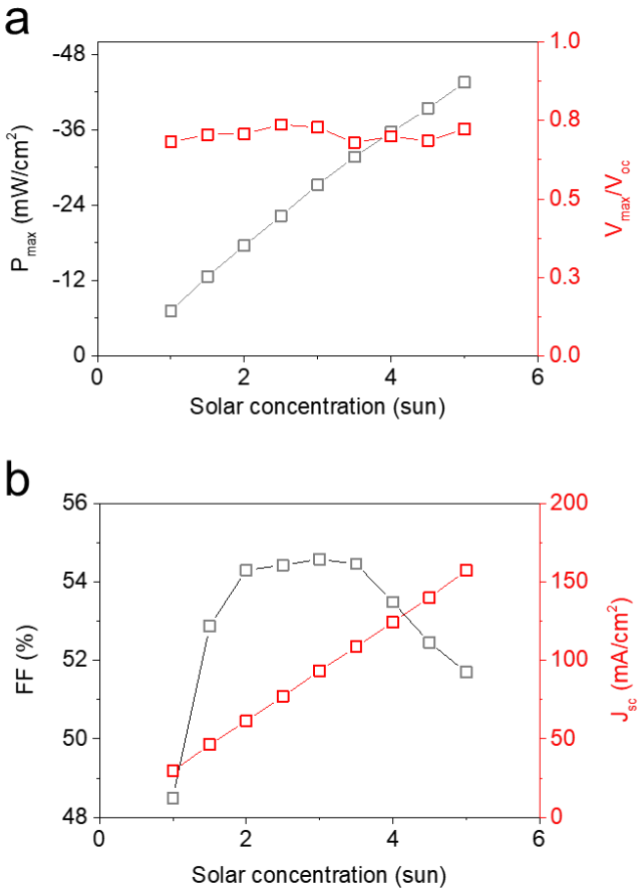

Figure S12. a) The MPP point and Vmax to V_{OC} ratio at different solar concentration. b) The evolution of FF and Jsc as a function of solar concentration.

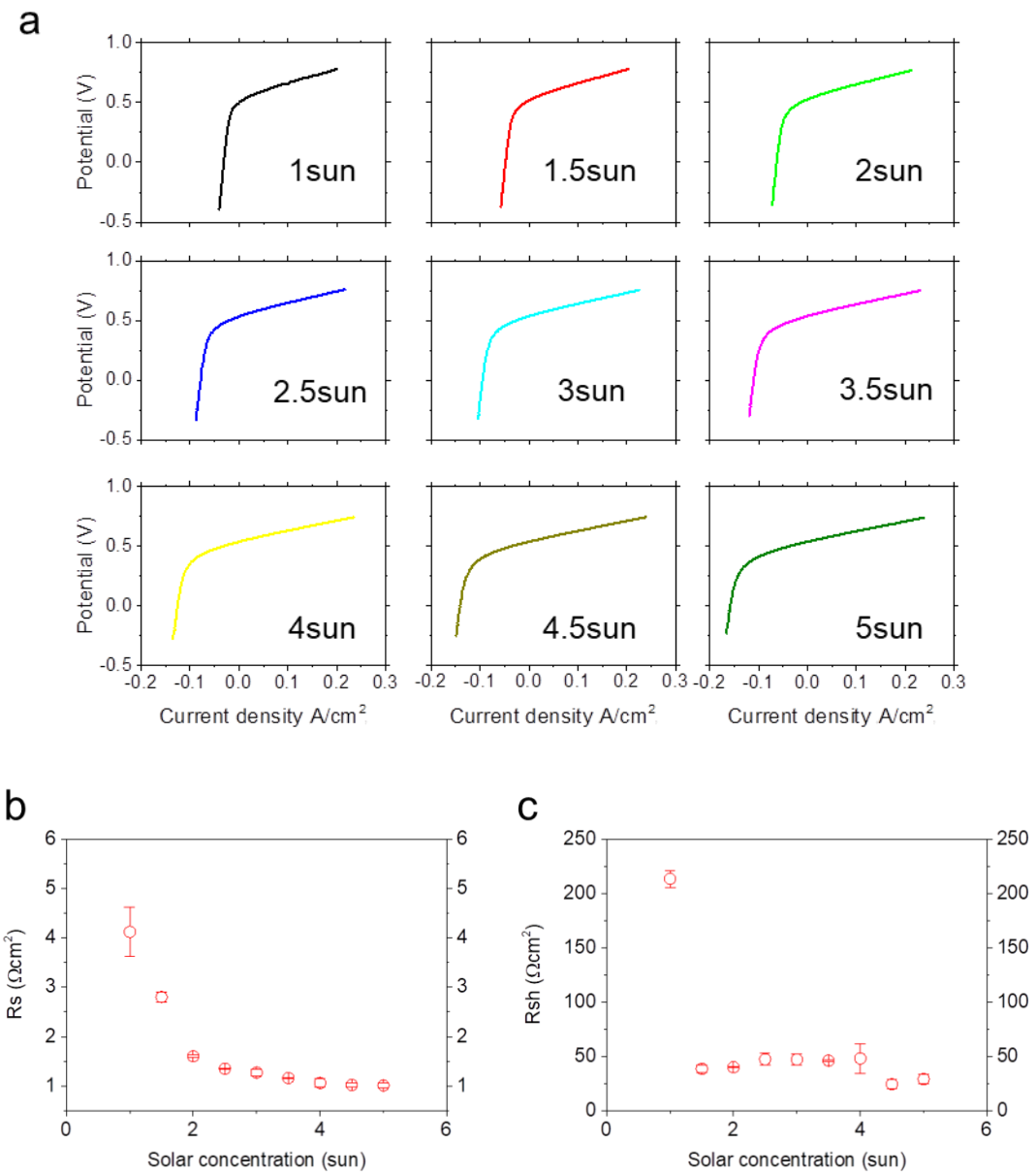

Figure S13. a) V-J curves of QDSC under different solar concentrations which were used for extracting series resistance (*Rs*) and shunt resistance (*Rsh*). b,c) Rs and Rsh evolution as a function of solar concentration.

Table S4 Summary of low-concentration QD photovoltaic parameters (1-3 Suns)					
	1 Sun (100 mWcm^{-2})	1.5 Suns (150 mWcm^{-2})	2 Suns (200 mWcm-^{2})	2.5 Suns (250 mWcm^{-2})	3 Suns (300 mWcm^{-2})
power conversion efficiency (*PCE*)	8.52±1.03% (9.55)	10.6±0.65% (11.25)	10.27±0.6% (10.87)	10.09±0.58% (10.67)	10.0±0.48% (10.48)
fill factor (*FF*)	48.5%	52.87%	54.3%	54.43%	54.58%
ideality factor (*n*)	0.82	0.82	0.82	0.82	0.82
short circuit current density (J_{sc})	29.55 mA/cm^2	46.27 mA/cm^2	61.46 mA/cm^2	76.95 mA/cm^2	93.45 mA/cm^2
open circuit voltage (V_{oc})	0.5 V	0.52 V	0.53 V	0.53 V	0.54 V
series resistance (R_s)	4.12±1.5 Ωcm^2	2.8±1.1 Ωcm^2	1.6±0.03 Ωcm^2	1.35±0.01 Ωcm^2	1.27±0.07 Ωcm^2
shunt resistance (R_{sh})	213.3±7.7 Ωcm^2	38.47±3.6 Ωcm^2	40±0.2 Ωcm^2	47.3±5.6 Ωcm^2	47.07±4.9 Ωcm^2

Continue Table S4 summary of low-concentration QD photovoltaic parameters (3-5 Suns)				
	3.5 Suns (350 mWcm^{-2})	4 Suns (400 mWcm^{-2})	4.5 Suns (450 mWcm-^{2})	5 Suns (500 mWcm^{-2})
power conversion efficiency (*PCE*)	9.93±0.48% (10.41)	9.82±0.45% (10.27)	9.7±0.45% (10.15)	9.545±0.46% (10.01)
fill factor (*FF*)	54.46%	53.49%	52.46%	51.7%
ideality factor (*n*)	0.82	0.82	0.82	0.82
short circuit current density (J_{sc})	108.65 mA/cm^2	124.35 mA/cm^2	140.05 mA/cm^2	157.35 mA/cm^2
open circuit voltage (V_{oc})	0.54 V	0.54 V	0.54 V	0.54 V
series resistance (R_s)	1.16±0.01 Ωcm^2	1.06±0.09 Ωcm^2	1.02±0.05 Ωcm^2	1.01±0.05 Ωcm^2
shunt resistance (R_{sh})	46.05±0.59 Ωcm^2	48.08±23.64 Ωcm^2	24.20±4.2 Ωcm^2	28.94±4.28 Ωcm^2

SVI Polymer lens concentrator

Figure S14 a-e present the detail information about polymer lens concentrator simulations and detail parameters used in the simulations are listed in the Table S5.[14] Figure 14f shows the power output curve of as-prepared QDSC integrated with different polymer lens. The optical absorption spectra of QD solid film together with a polymer lens are shown in Figure S15a. The first exciton peak remains very well after covering by the polymer lens caption which indicates exciton dynamics of QD film did not alter when the light rays were converged. The photostability of QD concentrator PV (QDCPV) is evaluated by 6 hours continuous 1 sun insolation. As shown in Figure S15b-f, there is no significant device performance degradation during light exposure. Detail QDCPV device parameters are summarised in Table S6.

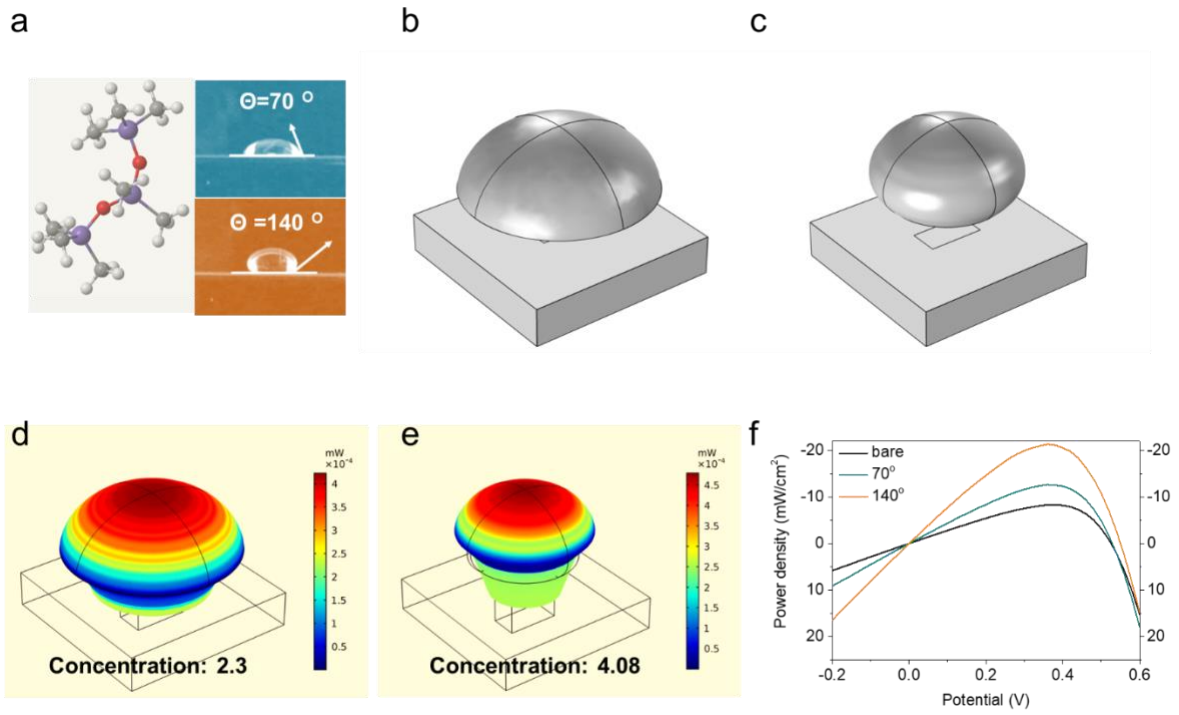

Figure S14. a) The molecule configuration of PDMS monomer and two CCD images of polymer lenses with different contact angles. 3D geometric profiles of 70° b) and 140° c) lens and simulated concentration ratios (d, e) employed for polymer solar concentrator. f) Power output curve of as-prepared QD polymer lens CPVs.

Table S5 Parameters for polymer lens concentrator simulation		
	70^{o}	140^{o}
Total emitted power density (mW/cm^2)	100	100
Total received power density (mW/cm^2)	102.91	106.68
Active area power density (mW/cm^2)	231.03	408.97

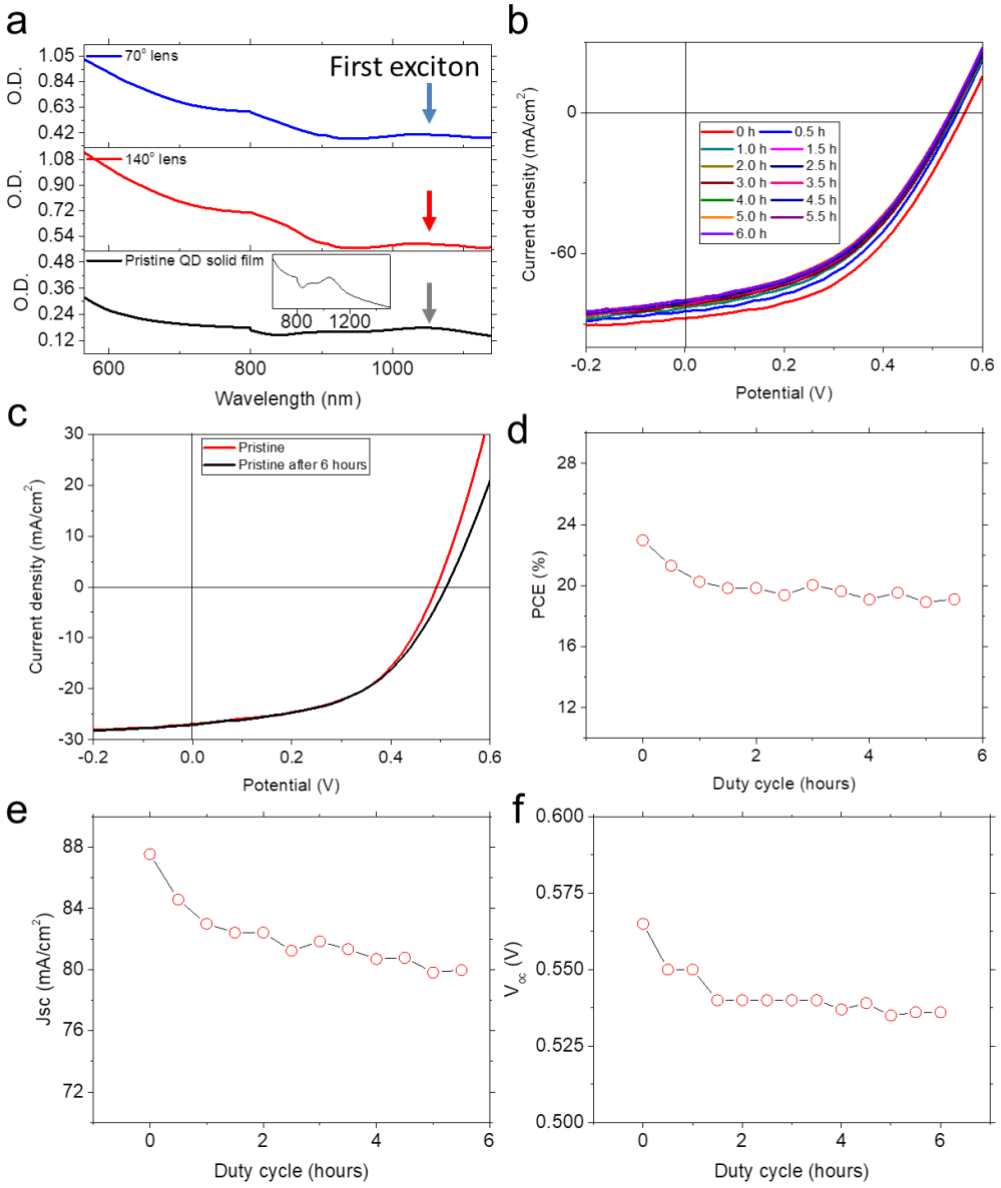

Figure S15. a) Optical absorption of QD solid film, QD solid film capped by 70° and 140° polymer lens. b) J-V curves of QDCPV capped by 140° polymer lens for 6 hours 1 Sun irradiance. c) J-V curves of QDCPV before and after 6 hours of light exposure. PCE d), J_{sc} e) and V_{oc} f) evolution trend as a function of exposure time.

Table S6 Summary of polymer lens QD photovoltaic parameters			
	Pristine QDSC	70^{o} lens	140^{o} lens
Module power conversion efficiency (*MPCE*)	8.31%	12.6%	21.3%
fill factor (*FF*)	0.56	0.54	0.49
Module short circuit current density (MJ_{sc})	28.42 mA/cm^2	44.56 mA/cm^2	79.99 mA/cm^2
open circuit voltage (V_{oc})	0.52 V	0.52 V	0.54 V
series resistance (R_s)	3.84 Ωcm^2	2.9 Ωcm^2	2.21 Ωcm^2
shunt resistance (R_{sh})	337.52 Ωcm^2	141.2 Ωcm^2	27.9 Ωcm^2

SVII Water lens concentrator

Mixers of H_2O and ethanol were used to generate different curvature water drops on a hexamethyldisilazane (HMDS) modified glass substrate (reverse side of ITO) to mimic the function of the solar concentrator. Figure S16 (a-d) shows a series of water lens with different ethanol volume concentration on hexamethyldisilazane (HMDS)-modified glass. It is well known that the wettability of a surface can be modified by the adsorption of the ethanol molecules on a liquid-vapor and liquid-solid interface.[15,16] The increased ethanol concentration changed the wettability of the HMDS-modified surface, resulting in a decreased wetting angle of water lens. Therefore, by adding these solution drops on the top of QDSC, artificial QD CPV can be easily fabricated. These water-based QD CPV show photon energy harvesting enhancement as exhibited in Figure S16e, which produce prominent power output comparing to bare QDSC (Figure S16f). Detail water-based QDCPV device parameters are summarised in Table S7.

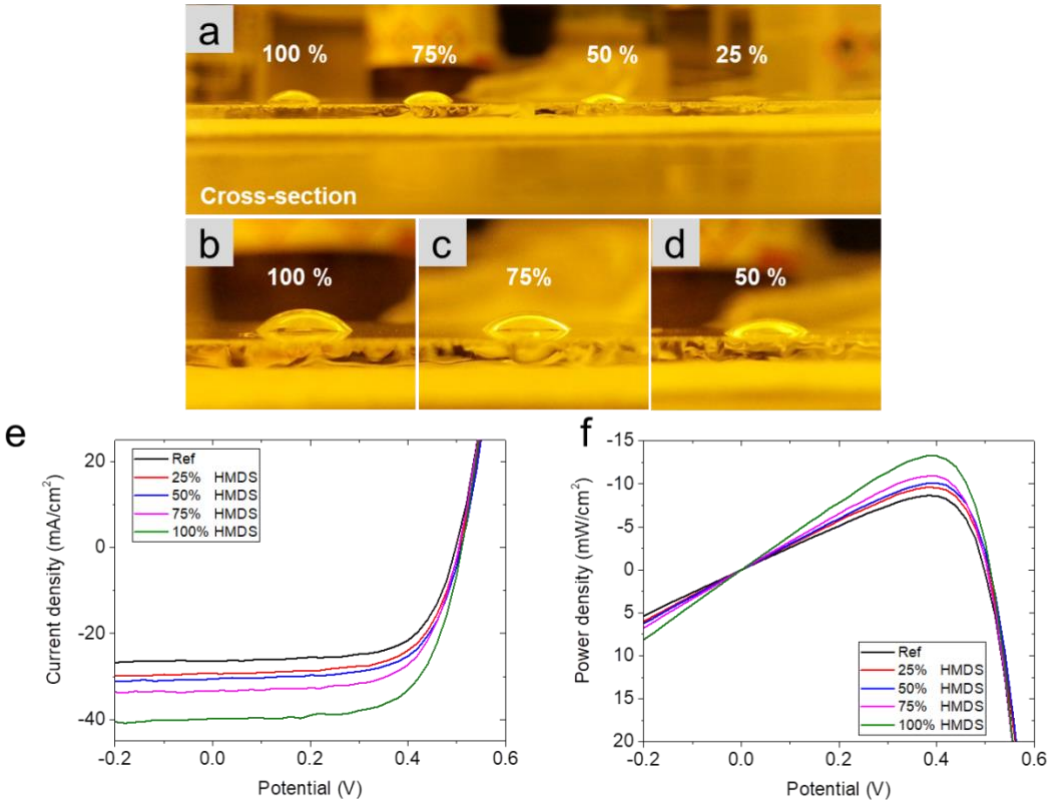

Figure S16. a) Cross-section view images of water drops having a different amount of ethanol on HMDS treated ITO substrate. b-c) enlarged CCD cross-section images. *J-V* e) and *P-V* f) curves of water-based QD CPVs.

Table S7 summary of water lens QD photovoltaic parameters					
	Pristine QDSC	25%	50%	75%	100%
module power conversion efficiency (*MPCE*)	8.64%	9.60%	10.10%	10.92%	13.28%
fill factor (*FF*)	0.6553	0.6554	0.6629	0.6555	0.6423
short circuit current density (J_{sc})	26.38 mA/cm^2	29.31 mA/cm^2	30.48 mA/cm^2	33.33 mA/cm^2	39.76 mA/cm^2
open circuit voltage (V_{oc})	0.50 V	0.50 V	0.50 V	0.50 V	0.52 V
series resistance (R_s)	2.25 Ωcm^2	2.37 Ωcm^2	2.42 Ωcm^2	2.06 Ωcm^2	1.49 Ωcm^2
shunt resistance (R_{sh})	171.35 Ωcm^2	529.43 Ωcm^2	246.19 Ωcm^2	181 Ωcm^2	179.48 Ωcm^2

SVIII A summary of the state-of-the-art PbS QD solar cells

Table S8 A summary of the state-of-the-art PbS QD solar cells						
Fabrication method	Irradiance	Jsc (mA/cm^2)	Voc (V)	FF (%)	PCE (%)	Reference
Solution-state ligand exchange	1 sun	29.1	0.64	70	13	[17]
Solution-state ligand exchange	1 sun	29.5	0.64	66	12.5	[18]
Solution-state ligand exchange	1 sun	30.2	0.65	68	13.3	[19]
QD/OPV hybrid	1 sun	29.6	0.66	67	13.1	[20]
Solution-state ligand exchange	1 sun	26.1	0.53	58.1	8.1	[21]
Solution-state ligand exchange	IR region	3.2	0.43	65.2	0.9	[21]
Solid-state ligand exchange	1 sun	25.2	0.61	59	9.1	[22]
Solid-state ligand exchange	1 sun	21.9	0.635	51	7.0	[23]
Solid-state ligand exchange	1 sun	25.3	0.633	66.8	10.4	[23]
Solid-state ligand exchange	IR region	3.44	0.32	61	0.67	[24]
Solid-state ligand exchange	1 sun	25.84	0.63	68.8	11.21	[25]

Solid-state ligand exchange	1 sun	29.55	0.5	48.5	8.52±1.03 (9.55)	This work
Solid-state ligand exchange	Indoor (2000 Lux)	0.4238	0.36	69.4	19.2±0.3 (19.5)	This work
Solid-state ligand exchange	1.5 sun	46.27	0.52	52.87	10.6±0.65 (11.25)	This work
Solid-state ligand exchange	Polymer lens (4.08 sun)	79.99	0.54	49	21.3	This work

SIV Universal irradiance QDSC performance in different latitudes

The simulated QDSC performance among Hilo, Palm Springs, Seattle, Juneau are based on their hourly statistics annual irradiance data which were extracted from USA National Renewable Energy Laboratory (NREL) National Solar Radiation Database 1991–2010 as listed in the Table S8. We simulate our QDSC performance from actual daily irradiance among various latitudes (LA) to further quantify the emerging use of QDSCs under the different light conditions. By using a least squares algorithm, the polynomial from these variables (J_{sc}, V_{oc}, PCE) can be determined and empirical regression equations correlated to the PCE (Figure S17) can be computed (solid fitting lines). Therefore, given different LA insolation, the PV power can be readily simulated. It should be noted that these approximations are based on a constant FF (mean value 58.4%) and incident flux independent dark current condition.[6,12] As shown in Figure 4c, mean daily annual solar irradiance as a function of the month from four different USA cities are selected. These four towns (Hilo, Palm spring, Seattle and Juneau) have represented latitude degrees across the northern hemisphere.[26] It can be seen that there is a clear daily solar irradiance difference between these latitudes and they are all deviated from one Sun condition. However, as highlighted from the periphery of the contour map of Figure 4c, when we superimpose our QDSC into these cities, a similar PCE can be obtained regardless of the LA difference.

Furthermore, simulated indoor QDSC power generation between 7pm-24pm among these four cities as a function of irradiance is shown in Figure S18. Furthermore, QDSC measurement protocols are provided in Figure S19 and Table S9. These protocols were used for evaluating QDSC performance and stability under sunlight, indoor-light, and high-intensity light irradiance.

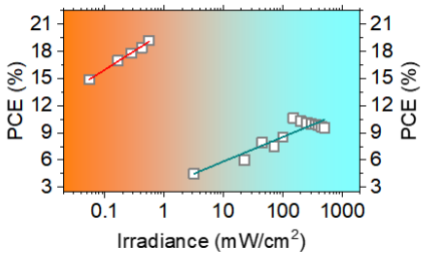

Figure S17. Least squares algorithm fitted lines for PCE evolution under variable ambient (indoor) and solar (sunlight, high light) irradiance.

Table S9 Annual hourly based solar irradiance (mW/cm^2) Hilo, Hawaii, Latitude: 19.717, Longitude: -155.05, TZ:-10																								
Time / Month	0	1	2	3	4	5	6	7	8	9	10	11	12	13	14	15	16	17	18	19	20	21	22	23
January	0	0	0	0	0	0	0	5.8	21.3	38.2	54	60.3	63.1	62.1	50.8	34.2	20.2	4.2	0	0	0	0	0	0
February	0	0	0	0	0	0	0.1	6.8	22.6	41.9	58.7	70	68.6	68.8	56.6	40.6	24.5	9.8	0.3	0	0	0	0	0
March	0	0	0	0	0	0	0.5	9.9	25.1	41.2	56.9	66.3	68.2	63.2	55.8	41	25.4	12.5	0.5	0	0	0	0	0
April	0	0	0	0	0	0	3.4	16.3	33.6	51.6	63.5	76.3	77.7	75.2	63.1	51.3	28.8	13.1	0.6	0	0	0	0	0
May	0	0	0	0	0	0.1	7.5	23.5	40.5	62.7	68.9	78.9	77.4	77.1	58.4	44.8	33.5	14.4	1.7	0	0	0	0	0
June	0	0	0	0	0	0.2	7.2	21.7	36	56.2	76.8	78.4	86.2	84.5	71.2	55.5	34.6	15.8	2.8	0	0	0	0	0
July	0	0	0	0	0	0.1	6.3	20.1	41.1	60	73.7	83	80.8	81.4	71.6	56.6	39.4	20.2	4	0	0	0	0	0
August	0	0	0	0	0	0	4	21.2	33.9	53.8	75.6	85	85.8	83.9	78	60	37.7	16.9	1.8	0	0	0	0	0
September	0	0	0	0	0	0	3.2	18.8	37.2	57.1	74	78.9	85.4	81	71.6	52.6	32	10	0.3	0	0	0	0	0
October	0	0	0	0	0	0	1.3	13.4	30.5	43.3	53.5	68.7	65	65.8	51.4	35.5	19.4	3.3	0	0	0	0	0	0
November	0	0	0	0	0	0	0.5	12.5	28.7	43.3	58.3	60.8	56.5	55.3	44.6	30.9	16	1.2	0	0	0	0	0	0

December	0	0	0	0	0	0	0.1	8	24	38.5	46.3	53.7	55	50.4	42.9	27.2	14.4	1.4	0	0	0	0	0	0
January	0	0	0	0	0	0	2.8	14.8	31.2	49	63.3	71.7	72.5	70.7	59.7	44.2	27.2	10.2	1	0	0	0	0	0

Continue Table S9 Annual hourly based solar irradiance (mW/cm^2) Palm Springs, CA, Latitude: 33.833˚, Longitude: -116.5˚ , TZ:-8

Time / Month	0	1	2	3	4	5	6	7	8	9	10	11	12	13	14	15	16	17	18	19	20	21	22	23
January	0	0	0	0	0	0	0.1	8.1	24.4	35.7	46.6	53	50.6	44.1	32.6	19.1	3.7	0	0	0	0	0	0	0
February	0	0	0	0	0	0	0.7	13.4	29.9	47	59	67.4	68.9	58.5	47.4	31.2	12.9	0.7	0	0	0	0	0	0

March	0	0	0	0	0	0.1	8.1	28.7	48.6	65.9	78	81.7	81	74.7	60.3	42.7	22.8	3.3	0	0	0	0	0	0
April	0	0	0	0	0	2.4	19.6	41.3	62.4	78.9	89.9	95.5	91	84.1	68.4	52.6	29.2	9.4	0.2	0	0	0	0	0
May	0	0	0	0	0.2	9	29.1	50.6	70.2	85.5	92.2	99.5	97	90.7	76.8	58.1	36.2	15.5	1.3	0	0	0	0	0
June	0	0	0	0	0.5	11.6	32.2	52.8	71.4	86.8	97.1	100.4	100.2	92.8	80	62.5	41.1	20.3	2.9	0	0	0	0	0
July	0	0	0	0	0.1	7.9	25.1	46.5	64.2	77.2	86.4	95.3	96.2	87.3	75.7	60.3	40.2	19.5	2.7	0	0	0	0	0
August	0	0	0	0	0	3.2	21.7	43.1	62.7	78.4	88.8	95.2	93.4	84	72.5	55.3	33.8	12.2	0.8	0	0	0	0	0
September	0	0	0	0	0	0.6	15.8	36.3	55.8	72.7	82.2	86.1	83.5	75.6	61.5	42.6	20.4	3	0	0	0	0	0	0
October	0	0	0	0	0	0.1	8.4	26.5	46.9	61.1	68.3	71.3	66.5	59.2	44.8	27	7.3	0.2	0	0	0	0	0	0
November	0	0	0	0	0	0	2.1	19.1	36.7	51.2	58.3	63.2	59.2	49	35.5	17.6	1.8	0	0	0	0	0	0	0
December	0	0	0	0	0	0	0.3	9	22.7	36.1	43.7	45.9	44.5	38.7	26.5	13.4	1.2	0	0	0	0	0	0	0
January	0	0	0	0	0.1	2.9	13.6	31.3	49.7	64.7	74.2	79.5	77.7	69.9	56.8	40.2	20.9	7	0.7	0	0	0	0	0

Continue Table S9 Annual hourly based solar irradiance (mW/cm^2) Seattle Boeing Field, WA, Latitude: 47.68˚, Longitude: -122.25˚, TZ:-8																								
Time / Month	0	1	2	3	4	5	6	7	8	9	10	11	12	13	14	15	16	17	18	19	20	21	22	23
January	0	0	0	0	0	0	0	0	2.8	8.7	12.6	15.6	15.3	14.7	10.3	6.9	0.9	0	0	0	0	0	0	0
February	0	0	0	0	0	0	0	1.5	10.7	19	26.2	31.6	29.1	29.4	24	18.9	7.7	0.6	0	0	0	0	0	0
March	0	0	0	0	0	0	1	8.7	18.9	27.9	35.4	41.2	40.8	41.2	32.6	24.5	15.2	5.6	0.2	0	0	0	0	0
April	0	0	0	0	0	0.9	7.8	17.5	27.5	37	43.4	43.8	48.6	47.7	37.4	30.6	22.5	11.2	2.5	0	0	0	0	0
May	0	0	0	0	0.2	4.1	13.8	26	36.2	46.7	54.1	56.3	52.9	50.1	47.3	40.7	27.5	19.2	8	0.6	0	0	0	0
June	0	0	0	0	0.6	5.5	16.8	26.6	34.9	46.6	53	54.8	58.8	54.4	54.5	44.4	30.4	19.9	11.6	2.7	0	0	0	0
July	0	0	0	0	0.2	5.6	15.4	25.7	39.1	49.9	56.9	70.3	76.4	71.2	65.9	58	45.2	29.9	14.3	2.9	0	0	0	0

August	0	0	0	0	0	1.5	9.7	20.7	32.4	41.5	52.2	62.5	66.5	63.3	58.1	50.1	35.4	19.9	5.7	0.2	0	0	0	0
September	0	0	0	0	0	0.1	3.9	13.3	19.8	28.6	34.7	40.3	47.2	40.6	35.5	28.1	17.5	6.1	0.3	0	0	0	0	0
October	0	0	0	0	0	0	0.5	8	18.7	27.3	33.6	35.4	31.3	30.7	25.5	15.7	5.6	0.3	0	0	0	0	0	0
November	0	0	0	0	0	0	0	1.3	7.9	12	16.7	17	16.7	15.2	11.8	5.6	0.4	0	0	0	0	0	0	0
December	0	0	0	0	0	0	0	0	3.5	9	11.9	16.8	17.1	13.8	10.2	4	0.1	0	0	0	0	0	0	0
January	0	0	0	0	0.1	1.5	5.7	12.4	21	29.5	35.9	40.5	41.7	39.4	34.4	27.3	17.4	9.4	3.6	0.5	0	0	0	0

Continue Table S9 Annual hourly based solar irradiance (mW/cm^2) Juneau INT'L ARPT, AK, Latitude: 58.35˚, Longitude: -134.583˚, TZ:-9

Time / Month	0	1	2	3	4	5	6	7	8	9	10	11	12	13	14	15	16	17	18	19	20	21	22	23
January	0	0	0	0	0	0	0	5.8	21.3	38.2	54	60.3	63.1	62.1	50.8	34.2	20.2	4.2	0	0	0	0	0	0

February	0	0	0	0	0	0	0.1	6.8	22.6	41.9	58.7	70	68.6	68.8	56.6	40.6	24.5	9.8	0.3	0	0	0	0	0
March	0	0	0	0	0	0	0.5	9.9	25.1	41.2	56.9	66.3	68.2	63.2	55.8	41	25.4	12.5	0.5	0	0	0	0	0
April	0	0	0	0	0	0	3.4	16.3	33.6	51.6	63.5	76.3	77.7	75.2	63.1	51.3	28.8	13.1	0.6	0	0	0	0	0
May	0	0	0	0	0	0.1	7.5	23.5	40.5	62.7	68.9	78.9	77.4	77.1	58.4	44.8	33.5	14.4	1.7	0	0	0	0	0
June	0	0	0	0	0	0.2	7.2	21.7	36	56.2	76.8	78.4	86.2	84.5	71.2	55.5	34.6	15.8	2.8	0	0	0	0	0
July	0	0	0	0	0	0.1	6.3	20.1	41.1	60	73.7	83	80.8	81.4	71.6	56.6	39.4	20.2	4	0	0	0	0	0
August	0	0	0	0	0	0	4	21.2	33.9	53.8	75.6	85	85.8	83.9	78	60	37.7	16.9	1.8	0	0	0	0	0
Septembe r	0	0	0	0	0	0	3.2	18.8	37.2	57.1	74	78.9	85.4	81	71.6	52.6	32	10	0.3	0	0	0	0	0
October	0	0	0	0	0	0	1.3	13.4	30.5	43.3	53.5	68.7	65	65.8	51.4	35.5	19.4	3.3	0	0	0	0	0	0
November	0	0	0	0	0	0	0.5	12.5	28.7	43.3	58.3	60.8	56.5	55.3	44.6	30.9	16	1.2	0	0	0	0	0	0
December	0	0	0	0	0	0	0.1	8	24	38.5	46.3	53.7	55	50.4	42.9	27.2	14.4	1.4	0	0	0	0	0	0
January	0	0	0	0	0	0	2.8	14.8	31.2	49	63.3	71.7	72.5	70.7	59.7	44.2	27.2	10.2	1	0	0	0	0	0

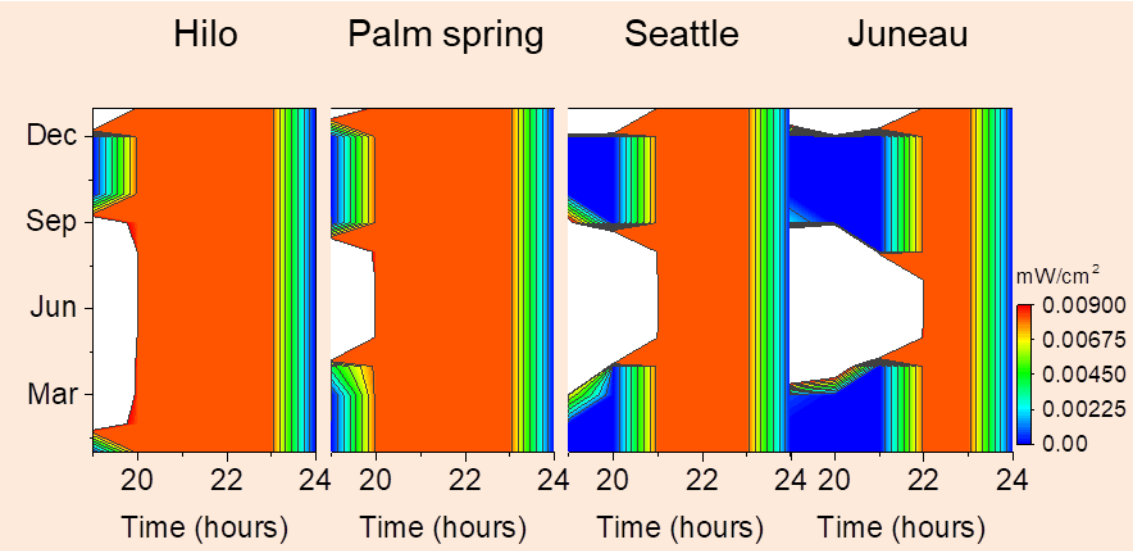

Figure S18. Simulated QDSC indoor power generation between 7 pm to 24 pm.

SX Solar cell measurement protocols.

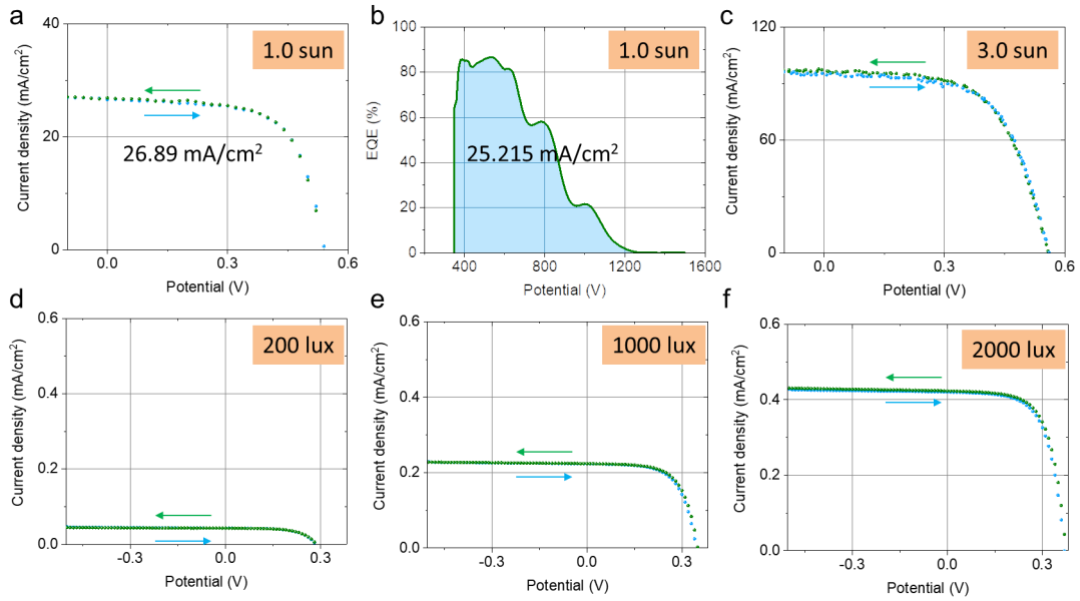

Figure S19. Test protocols of the QDSCs. Instantaneous forward and backward scanning J-V curves obtained under 1.0 Sun (a), 3.0 Sun (c), 200 lux (d), 1000 lux (e) and 2000 lux (f). Representative EQE spectrum provided in (b) was obtained with the same aperture mask for evaluating spectra and area mismatch (2.23 ± 0.91 mA/cm^2).[27] There is no considerable hysteresis effect observed in all QDSC devices under sunlight or indoor light. As widely reported, the QDSC generally show hysteresis-free and stable in air under sunlight.[28,29] Under high-intensity light irradiation, there is slightly hysteresis present due to thermal effect and the only backward scan is extracted for the rest of discussion.[30-32]

Table S10. Comparisons of the spectral mismatch between EQE and solar simulator system.[27]

J_{sc} (mA/cm^2)	J_{sc} (EQE) (mA/cm^2)	Mismatch (mA/cm^2)
27.55 ± 1.15	25.32 ± 1.43	2.23 ± 0.91

Reference

1 Hou, B. *et al.* Structure and Band Edge Energy of Highly Luminescent CdSe1–xTex Alloyed Quantum Dots. *J. Phys. Chem. C* **117**, 6814-6820 (2013).

2 Hou, B. *et al.* Highly Monodispersed PbS Quantum Dots for Outstanding Cascaded-Junction Solar Cells. *ACS Energy Lett.* **1**, 834-839 (2016).

3 Ellingson, R. J. *et al.* Highly Efficient Multiple Exciton Generation in Colloidal PbSe and PbS Quantum Dots. *Nano Lett.* **5**, 865-871, doi:10.1021/nl0502672 (2005).

4 Kang, I. & Wise, F. W. Electronic structure and optical properties of PbS and PbSe quantum dots. *J. Opt. Soc. Am. B* **14**, 1632-1646 (1997).

5 Wei, S.-H. & Zunger, A. Electronic and structural anomalies in lead chalcogenides. *Phys. Rev. B* **55**, 13605-13610 (1997).

6 Lee, H. K. H., Li, Z., Durrant, J. R. & Tsoi, W. C. Is organic photovoltaics promising for indoor applications? *Appl. Phys. Lett.* **108**, 253301 (2016).

7 Memming, R. *Semiconductor Electrochemistry*. (Wiley, 2015).

8 Cowan, S. R., Roy, A. & Heeger, A. J. Recombination in polymer-fullerene bulk heterojunction solar cells. *Phys. Rev. B* **82**, 245207 (2010).

9 Kirchartz, T., Deledalle, F., Tuladhar, P. S., Durrant, J. R. & Nelson, J. On the Differences between Dark and Light Ideality Factor in Polymer:Fullerene Solar Cells. *J. Phys. Chem. Lett.* **4**, 2371-2376 (2013).

10 Husain, M. A., Tariq, A., Hameed, S., Arif, M. S. B. & Jain, A. Comparative assessment of maximum power point tracking procedures for photovoltaic systems. *Green Energy Environ.* **2**, 5-17 (2017).

11 Mathews, I., Kelly, G., King, P. J. & Frizzell, R. in *2014 IEEE 40th Photovoltaic Specialist Conference (PVSC).* 0510-0513.

12 Nelson, J. *The Physics of Solar Cells*. (Imperial College Press, 2003).

13 Sacco, A. *et al.* Dye-sensitized solar cell for a solar concentrator system. *Solar Energy* **125**, 307-313 (2016).

14 Jeter, S. M. Calculation of the concentrated flux density distribution in parabolic trough collectors by a semifinite formulation. *Solar Energy* **37**, 335-345 (1986).

15 Vázquez, G., Alvarez, E., Rendo, R., Romero, E. & Navaza, J. M. Surface Tension of Aqueous Solutions of Diethanolamine and Triethanolamine from 25 °C to 50 °C. *J. Chem. Eng. Data* **41**, 806-808 (1996).

16 Yonemoto, Y. & Kunugi, T. Experimental and theoretical investigation of contact-angle variation for water–ethanol mixture droplets on a low-surface-energy solid. *Int. J. Heat Mass Transfer* **96**, 614-626 (2016).

17 Biondi, M. *et al.* A Chemically Orthogonal Hole Transport Layer for Efficient Colloidal Quantum Dot Solar Cells. *Adv. Mater.* **32**, 1906199, doi:10.1002/adma.201906199 (2020).

18 Sun, B. *et al.* Ligand-Assisted Reconstruction of Colloidal Quantum Dots Decreases Trap State Density. *Nano Lett.* **20**, 3694-3702, doi:10.1021/acs.nanolett.0c00638 (2020).

19 Choi, M.-J. *et al.* Cascade surface modification of colloidal quantum dot inks enables efficient bulk homojunction photovoltaics. *Nat. Commun.* **11**, 103, doi:10.1038/s41467-019-13437-2 (2020).

20 Baek, S.-W. *et al.* Efficient hybrid colloidal quantum dot/organic solar cells mediated by near-infrared sensitizing small molecules. *Nature Energy* **4**, 969-976, doi:10.1038/s41560-019-0492-1 (2019).

21 Kim, Y. *et al.* A Facet-Specific Quantum Dot Passivation Strategy for Colloid Management and Efficient Infrared Photovoltaics. *Adv. Mater.* **31**, 1805580, doi:10.1002/adma.201805580 (2019).

22 Hu, L. *et al.* Achieving high-performance PbS quantum dot solar cells by improving hole extraction through Ag doping. *Nano Energy* **46**, 212-219, doi:https://doi.org/10.1016/j.nanoen.2018.01.047 (2018).

23 Teh, Z. L. *et al.* Enhanced Power Conversion Efficiency via Hybrid Ligand Exchange Treatment of p-Type PbS Quantum Dots. *ACS Appl. Mater. Interfaces* **12**, 22751-22759, doi:10.1021/acsami.9b23492 (2020).
24 Bi, Y. *et al.* Infrared Solution-Processed Quantum Dot Solar Cells Reaching External Quantum Efficiency of 80% at 1.35 μm and Jsc in Excess of 34 mA cm−2. *Adv. Mater.* **30**, 1704928, doi:10.1002/adma.201704928 (2018).
25 Lu, K. *et al.* High-Efficiency PbS Quantum-Dot Solar Cells with Greatly Simplified Fabrication Processing via "Solvent-Curing". *Adv. Mater.* **30**, 1707572, doi:10.1002/adma.201707572 (2018).
26 The irradiance is collected from USA National Solar Radiation Database 1991–2010.
27 Data were extracted across 20 samples. The current density of EQE system was integrated under AM1.5G TILT (ASTM-G173-03) with solar cell mask area 0.012 cm2. Jsc = (Jsc-forward + Jsc-backward)/2.
28 Xu, J. *et al.* 2D matrix engineering for homogeneous quantum dot coupling in photovoltaic solids. *Nature Nanotechnology*, doi:10.1038/s41565-018-0117-z (2018).
29 Liu, M. *et al.* Hybrid organic-inorganic inks flatten the energy landscape in colloidal quantum dot solids. *Nat. Mater.* **16**, 258-263 (2017).
30 Yandt, M. D., Cook, J. P. D., Kelly, M., Schriemer, H. & Hinzer, K. Dynamic Real-Time I-V Curve Measurement System for Indoor/Outdoor Characterization of Photovoltaic Cells and Modules. *IEEE J. Photovolt.* **5**, 337-343, doi:10.1109/JPHOTOV.2014.2366690 (2015).
31 Gordon, J. M., Katz, E. A., Tassew, W. & Feuermann, D. Photovoltaic hysteresis and its ramifications for concentrator solar cell design and diagnostics. *Appl. Phys. Lett.* **86**, 073508, doi:10.1063/1.1862776 (2005).
32 Speirs, M. J. *et al.* Temperature dependent behaviour of lead sulfide quantum dot solar cells and films. *Energy Environ. Sci.* **9**, 2916-2924, doi:10.1039/C6EE01577H (2016).